Spatiotemporal temperature and chlorophyll-a mapping and modeling in the Gulf of Corinth using Landsat satellite imagery

Naomi Krauzig

MASTERS DESSERTATION

Supervisor: Prof. Vassilis Zervakis

Mytilene, September 2017

Dissertation submitted in fulfillment for the Degree of Master of Science in Integrated Coastal Management

Graduate of the Department of Marine Sciences

Naomi Krauzig

THESIS TOPIC:

Spatiotemporal temperature and chlorophyll-a mapping and modeling in the Gulf of Corinth using Landsat satellite imagery

Examination Committee		Signatures
Advisor:	Prof. Vassilis Zervakis	
First Examiner:	Prof. Elina Tragou	
Second Examiner:	Prof. Evangelia Krasakopoulou	

Declaration

I have read and understood the rules on cheating, plagiarism and appropriate referencing and I declare that the work contained in this assignment is my own, unless otherwise acknowledged.

No substantial part of the work submitted here has also been submitted by me in other assessments for this or previous degree courses, and I acknowledge that if this has been done an appropriate reduction in the mark I might otherwise have received will be made.

Signed candidate_____

Acknowledgements

Contents

Abstract

The effluent from a vertically integrated alumina and aluminum production and (since the late 2000s) thermal electric power production plant located on Antikyra bay in the Gulf of Corinth is being examined. This study processes satellite sea surface temperature and chlorophyll-a data and examines the possibility of thermal pollution from the aluminum processing plant considering the local geomorphology. The sea surface temperatures were derived from 58 Landsat 5 and 7 images from July 2009 until December 2016. Respectively, the Chl-a concentrations were retrieved using reflectance data of 6 Landsat OLI images from April 2014 until October 2015 in order to statistically correlate the various combinations of Landsat bands with in-situ measurements and to quantify algorithms that best describe this relationship and calculate accurately the concentration of chlorophyll-a. A polynomial model employing the band ratio B4/B1 was found to be the most efficient algorithm for the chlorophyll-a estimation of the Antikyra Bay with a maximum correlation coefficient of $R^2 = 0.99$. Based on the correlation coefficients, the most sufficient local algorithm was found to be chl-a= $59.423x(b4/b1)^2-22.687x(b4/b1)+2.174$. The results confirmed the suitability of the method for assessing the concentration of chlorophyll-*a* in the Gulf of Corinth with statistical accuracy. Furthermore, the atmosphere influences on the sea surface temperature variation were indicated using air-sea heat flux data.

Περίληψη

Η μεταπτυχιακή εργασία εξετάσει την θερμική επιρροή ενός εργοστασίου επεξεργασίας αλουμινίου στον κόλπο των Αντικύρων του Κορινθιακού Κόλπου. Συγκεκριμένα αναλύονται δορυφορικά δεδομένα επιφανειακής θαλάσσιας θερμοκρασίας και χλωροφύλλης-α με λαμβάνοντας υπόψη την τοπική γεωμορφολογία. Τα δεδομένα επιφανειακής θερμοκρασίας λήφθηκαν από 58 δορυφορικές εικόνες του αισθητήρα Landsat 5 και 7 για την χρονική περίοδο Ιουλίου του 2009 μέχρι Δεκέμβριο του 2016. Αντίστοιχα, τα δεδομένα Chl-a ανακτήθηκαν χρησιμοποιώντας τιμές ανακλαστικότητας από 6 δορυφορικές εικόνες του αισθητήρα Landsat 8 από τον Απρίλιο του 2014 έως τον Οκτώβριο του 2015, προκειμένου να συσχετιστούν στατιστικά οι τιμές ανακλαστικότητας από πολλαπλούς συνδυασμούς μπαντών με in-situ μετρήσεις και να αναπτυχθεί τοπικός υψηλής ανάλυσης αλγόριθμος εκτίμησης της συγκέντρωσης της χλωροφύλλης-α. Διαπιστώθηκε ότι ο καλύτερος συνδυασμός των μπαντών για αυτό το σκοπό αποτελεί η αναλογία των μπαντών B4/B1 με τον μέγιστο συντελεστή συσχέτισης να ισούται με $R^2=0.99$. Ο αποτελεσματικότερος, αντίστοιχα αλγόριθμος βρέθηκε ότι είναι chl-a=$59.423x(b4/b1)^2-22.687x(b4/b1)+2.174$. Επιπλέον εξετάστηκαν οι επιδράσεις της ατμόσφαιρας στις διακυμάνσεις της επιφανειακής θερμοκρασίας της θάλασσας αναλύοντας δεδομένα ροής θερμότητας από το Εθνικό Κέντρο Ατμοσφαιρικής Πρόγνωσης (NCEP) και το Εθνικό Κέντρο Έρευνας της Ατμόσφαιρας (NCAR).

1.) Introduction

Coastal areas are often used as a disposal environment for thermal effluents originating from the cooling processes in industry plants. However, the problem of natural water bodies' thermal pollution is usually and unjustifiably neglected. Any change in water temperature of the natural water intake, due to human activity is so-called thermal pollution (Langfort, 1990; Bilge et al., 2015). Water temperature has a direct or indirect influence on aquatic water ecosystems and it plays a critical role affecting the distribution of phytoplankton and fish species, stock catch, and diversification of aquaculture, i.e. the presence crabs, shrimps, and molluscs in the water body. In fact, the modified water input can affect water temperature, and possibly locally modify stratification and dissolved oxygen concentration. This may have negative impact on fish and other macroscopic/microscopic organisms, and their quantitative and qualitative nature. As a result, these alterations in water inflows may negatively affect all the food chain from freshwater to marine environment (Poff et al. 1997). Water temperature affects the overall biological and chemical composition of a stream (Pluhowski 1970; Paul and Meyer 2001; Poole and Berman 2001). It influences nutrient cycles and productivity within fluvial systems (Allan and Castillo, 2007). For that purpose, the impact of thermal pollution due to manmade coastal structures is explicitly mentioned in the European Commission's Marine Strategy Framework Directive (2008/56/EC).

Temperature also affects the solubility of gases in water, such as O_2, CO_2, N_2 and CH_4. In warm waters, respiration and growth rates increase. As growth of bacteria and phytoplankton population occurs in a short period, the effect of rising water temperature is remarkable and algal blooms could be observed. For this reason, it is important to understand how water body temperature is affected by heated wastewater discharge.

It is also noteworthy that planktonic organisms are drawn along with the cooling water into the plant cooling circuit, where they are subjected to various physical and chemical stress factors. Moreover, organisms in the receiving water body may also be entrained into the effluent plume, even if they do not pass through the plant cooling circuit. Apart from increased temperature, the discharges often contain chemical stress factors in the form of biocides (e.g., chlorine) used for biofouling control (Morgan and Carpenter, 1978). Phytoplankton are a very important constituent of the coastal food chain and, therefore, qualitative and quantitative changes in the phytoplankton population in the receiving water body may have significant implications for the coastal ecosystem. As phytoplankton are drawn into the cooling circuit and then discharged back into the sea along with the effluents, it is possible that they suffer damages due to temperature and chlorine stress.

Industries like aluminum-processing plants, as well as fossil fuel and nuclear power plants use lots of water for cooling purposes and return this water to the environment at a higher temperature. These temperature changes may adversely affect aquatic ecosystems

especially by contributing to the decline of wildlife populations and habitat destruction. Any practice that affects the equilibrium of an aquatic environment may alter the temperature of that environment and subsequently cause thermal pollution. There may be some positive effects, though, to large-scale thermal pollution, including the extension of fishing seasons and rebounding of some wildlife populations.

At present one company in Greece, the "Aluminum of Greece S. A.", is active in bauxite extracting pure alumina (aluminum oxide) and aluminum. Since 2009, the company has extended the operation of the facilities to include production of electric energy via fossil fuel burning. The occurrence of thermal plumes in the wider coastal area near the power plant has been suggested to be connected to the cooling process of the factory.

The horizontal dispersion of thermal plumes is mainly driven by wind-induced currents (He et al., 2006; Choi and Wilkin, 2007; Cardoso-Mohedano et al., 2015). Near-shore regions close to the emitting source are therefore especially sensitive to thermal pollution since heat plumes can be trapped by coastal currents without being dispersed across the water body (Raithby et al., 1988; Salgueiro et al., 2015).

Many water management authorities have enforced three kinds of limitations to heat use: (i) a maximum temperature of water used for cooling, (ii) a maximum temperature increase in the natural waters receiving the thermal effluents, and (iii) a maximum temperature in the receiving waters. The latter condition will restrict the suitability of various waters as heat recipient under the perspective of climate change, due to the expected increase of water temperature as well as changes in discharge/rain patterns.

This work exploits satellite data and air-sea fluxes in order to examine whether the aluminum plant effluents the sea temperature and the chlorophyll-a concentration and in order to examine the spatiotemporal evolution of these parameters in the Gulf of the Corinth. Thus, below, the data and methodology used are presented after the introduction section (1) in section (2). The results are presented in section (3) and are summarized and discussed in the concluding section (4).

1.1.) The study area

The Gulf of Corinth is a topographically-restricted marine embayment, with an approximately 105 longitudinal axis lying in an E-W direction (Fig.1.). The Gulf extends from the strait of Rio - Antirrio (to the west), up to the gulf of Alkyonides in the east. The total length reaches 130 km, while its width ranges from 5 to 30 km. Its maximum depth is measured at ~900 m. From a geological point of view, the Corinthian Gulf is a submarine sedimentary basin and is part of the Corinthian tectonic fault. More specifically, it is the northernmost and currently the most active part of the moat. With a total area of approximately 2400 km² out of a total of 4100 km² occupied by the Corinthian moat, the Gulf continues to dilate and plunge.

Figure 1.) Landsat 5 satellite image of (a) Greece and (b) the Gulf of Corinth (ENVI 5.1.)

1.1.1.) Morphology

The morphology of the northern margin of the Gulf consists of a wide shelf, in Antikyra Bay, which passes through a steeping slope and ends to a deep basin floor at ~900 m water depth (Figure 2).
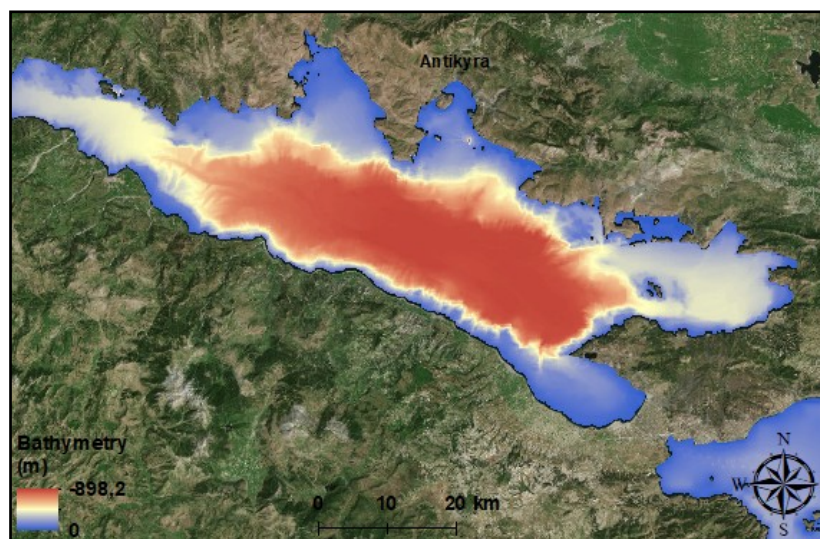
Fig. 2.) Bathymetric map of the area based on EMODnet bathymetry data, identifying the Antikyra bay (ArcGIS 10.2.2.)

The submarine bathymetry of the Gulf of Corinth consists of four main physiographic provinces:

1) the continental shelf
2) the continental slope
3) the continental rise
4) the abyssal plain

The system is completed by the Delphic Plateau and Alkionides Basin (Heezen et al., 1966). More specific, the northern continental shelf area extends into the central part of the Gulf into water depths of around 200 m (the shelf break); its width varies greatly at between 700 m and 12 km (Antikyra Bay) and it is associated with gentle slopes (Figure 3).

In contrast, the southern shelf is narrow (< 1 km) and is relatively steep, with the shelf break occurring at a water depth of about 100 m. The northern slope varies at between 3 and 7 km in width, whilst the southern slope is much narrower (1.5-2.5 km) and steeper. In the north, the continental rise is narrower and steeper than in the south, where the width ranges between 1 and 5.5 km. Finally, the abyssal plain occupies the middle part of the central basin at water depths about 900 m.

Figure 3.) 3D Elevation Model of the combined marine and land surface data, presenting the morphology of the Gulf of Corinth (GeoMapApp)

1.1.2.) Oceanographical setting

Published current data from the Gulf of Corinth are few, so that the understanding of water circulation is still incomplete. Strong currents have been measured at the entrance of the Gulf of Corinth, over the Rion sill area (~1.0 m s^{-1}) and over the Mornos–Drepano sill, located ca. 9 km further to the east (0.6 m s^{-1}) (Lascaratos et al., 1989). Modeling of the marine currents in the Gulf of Patras for different boundary conditions suggests that currents at the entrance of the Gulf of Corinth are generally controlled by tides, and occasionally by winds (Fourniotis and Horsch, 2012). Modeled rising tide-induced currents are unidirectional in

winter, but in summer, a cold-water bottom-current flows from the Gulf of Corinth to the Gulf of Patras, while a warmer current flows in an upper layer in the opposite direction (Fourniotis and Horsch, 2012). In the central gulf near-bed current-meter data and water-surface temperature analysis suggest that the velocity of the currents is very low (<8 cm s^{-1}, Poulos et al., 1996) and that a counterclockwise gyre is centered in this area (Lascaratos et al., 1989). The Gulf of Corinth waters show a thermal stratification in summer. The upper layer, from 0 to ~100 m exhibits a strong thermal gradient from 21 to 26 °C at the surface to ~13 °C just below the thermocline, while below 100m, the temperature is uniform at 13 °C. In winter, convection homogenizes the temperature profile to around 13 °C (Lascaratos et al., 1989; Poulos et al., 1996).

Also, Anderson and Carmack (1973) distinguished two major water masses present within the Gulf: a surface layer (0-200 m) wherein temperature and salinity vary seasonally with depth; and waters below 200 m, where the temperature and salinity remain almost constant with depth. Temperature and salinity within the surface water layer range between 25°C and 38.55 psu (summer) and 14.3°C and 38.35 psu (winter), respectively. Below 200 m, they remain almost constant at 13.3°C and 38.57 psu (summer) and 12.8°C and 38.41 psu (winter), respectively. The same investigators identified an intermediate layer with both temperature and salinity maximum lying at between 125 m and 175 m within the water column. Furthermore, they interpreted the former temperature and salinity maximum as the result of advection of Ionian Sea water over the Rion sill. In contrast, the deep water mass (below 200 m) is characterized by much lower temperatures and salinities compared with the open Ionian Sea; thus, it is formed locally by downward convection of the surficial water mass, during winter and early spring (Nielsen, 1912). Dissolved oxygen concentrations fluctuate seasonally, having their higher saturation values between February and August (Friligos et al., 1985) and with maximum saturation (>80%) just below the sea surface. Furthermore, the water column below 200 m and near the sea bed contains oxygen; this is indicative of active renewal processes i.e. overturning of the deep water mass, during winter.

The surface water circulation is dominated by the funneling of both wind and water through the narrow Rion Straits, where near-surface current velocities can exceed 100 cm/s (Piper et al., 1990). More specifically, the wind climate is characterized by the presence of a highly bi-modal pattern, with E and WSW winds dominating. Lascaratos et al. (1989), utilizing infrared satellite imagery, have identified the presence of an anti-clockwise gyre in the surface water circulation pattern of the central part of the Gulf, to the south of Antikyra Bay. The same investigators have identified also wind-induced summer upwelling along the northern shoreline of the Gulf.

According to Poulos et al. (1996) the Gulf of Corinth is a late Quaternary fault controlled basin. The deep water (> 900 m) basin is connected with the Gulf of Patras (and open Ionian

Sea) through straits incorporating a shallow sill (65 m), at its western end: there is an 8 m deep artificially-dredged channel (the Corinth canal) at the southeastern limit. Such conditions create a bathymetrically-restricted "fjord-like" marine embayment. The prevailing oceanographical setting of such an "isolated" environment is controlled by: (1) local climate; (2) freshwater runoff from the surrounding mountains; and (3) the limited exchange of waters over the western sill. Conversely, geological characteristics are related to intensive tectonic activity, with sedimentation processes controlled mainly by gravity-driven mass movements. The dissolved oxygen concentration increases with depth within the bottom water mass, indicating its localized formation by downward advection of surface waters. This process occurs during winter and early spring, when the surface waters become denser in response to a decrease in air temperature. Near-bed water circulation is associated with slow-moving currents, with maximum observed speeds of < 8 cm/s at a level of 5 m above the sea bed. The current regime is controlled by changes in atmospheric pressure, despite the relatively large water depths involved. Opposing flows along the northern and southern margins of the Gulf may represent the presence of an anti-clockwise gyre or eddy.

1.1.3.) Biodiverisity

On the side of Central Greece, the seabed is mainly rocky with clear waters and good visibility. This factor has resulted in the development of a rich biodiversity of marine flora and hence the development of a rich fauna. On the side of the Peloponnese, the seabed is mainly sandy and muddy, resulting mainly in migratory or seasonal fish populations. The two main surface streams recorded in the middle of the Corinthian Gulf are related to the transfer of planktonic organisms, but also to the presence of species such as tuna, swordfish and palamides. Despite its relatively small size, the Corinthian Gulf supports significant populations of marine mammals that either cross the sea waters or live permanently in them. According to recent research (Archipelagos NGO), the mammal species recorded are: *Tursiops truncatus, Stenella Coeruleoalba, Delphinus Delphis, Grampus griseus, Balaenoptera physalus*. At the same time, the shallow, coastal waters of the Corinthian Gulf support a rich biodiversity of species of fish, invertebrates and algae (*Padina pavonica, Peyssonnelia rubra, Corallina elongata, Laurencia obtusa, Jania rubens, Codium bursa, Halophila stipulacea, Acetabularia acetabulum, Cystoseira sp*.), as well as large areas of protected ecosystems, such as Posidonia meadows and coral reefs (*Eunicella cavolini, Paramuricea clavata, Leptogorgia sarmentosa*).

Due to its rich biodiversity and unique ecosystems and habitats, in the summer of 2016, the Corinthian Gulf was nominated by the Hellenic Ministry to be part of the Natura 2000 network. However, final designation is still pending. The same goes for the rest of the marine Natura sites of Greece that were nominated by the same Ministerial Decision.

1.1.4.) Meteorological setting

The climate near the Gulf of Corinth is typical for the Greece climate with mild and rainy winters, relatively warm and dry summers and extended periods of sunshine throughout most of the year.
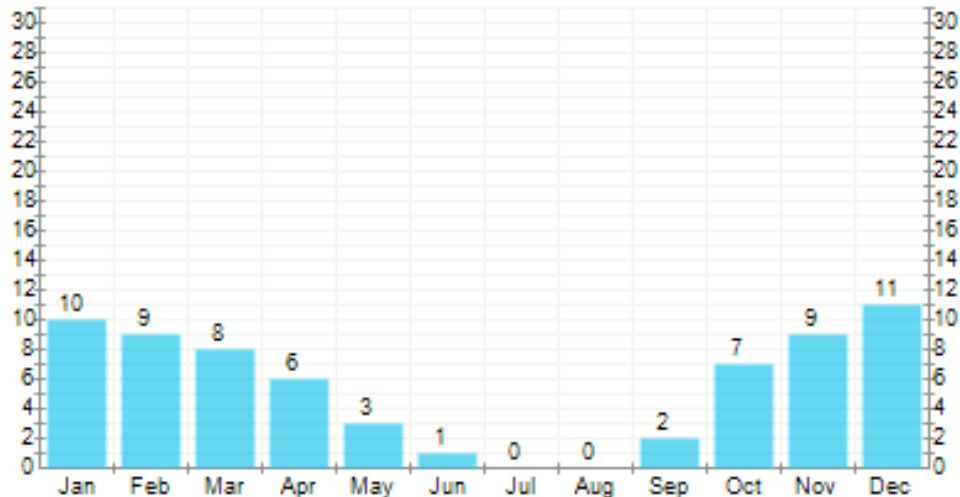
Fig.4.) Diagram with the average amount of days (24h) with precipitation during a month for the period 1961–1990. When precipitation has surpassed 1mm per day it is defined as a day with precipitation. (Data Source: World Meteorological Organization (WMO))
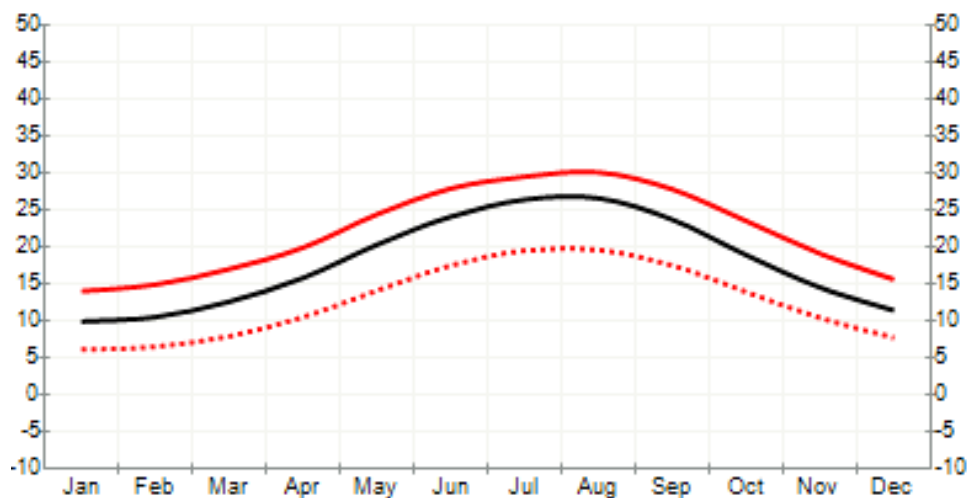
Fig.5.) The monthly temperature (red:max, black:average, dotted: minimum) measured in the period 1961–1999 for the meteorological station in Patras, Greece. (Data Source:WMO)

According to Andreadis et al. (2001) from the Hellenic National Meteorological Service, the year can be broadly subdivided into two main seasons: The cold and rainy period lasting from mid-October until the end of March, and the warm and dry season lasting from April until September During the first period the coldest months are January and February, with, a mean minimum temperature ranging, on average, between 5 -10 degrees Celsius near the coasts and 0 – 5 Celsius over the mainland. The warmest period occurs during the last ten days of July and the first ten days of August, when the mean maximum temperature lies between 29.0 and 35.0 degrees Celsius.

1.2.) The vertically-integrated alumina and aluminium production plant

The aluminum processing plant was established in 1960 as "ALUMINUM OF GREECE S.A." and today is Europe's most modern vertically integrated alumina and aluminium production and trading plant. With an annual output capacity reaching 810,000 tons of alumina, 165,000 tons of primary-cast aluminum (electrolysis) and 170,000 tons of finished aluminum (end-product), ALUMINIUM S.A. is the largest alumina and aluminum producer in SE Europe. Its facilities occupy a total area of around 7,000,000 m^2 and are located in Agios Nikolaos, on the coast of Distomon, Viotia.

Fig.6.) Satellite picture of the aluminum plant from Google Earth

Furthermore, since 2008, the same premises of the aluminum processing factory in Ag. Nikolaos, Viotia are used by the electricity power provider "Protergia", with the operation of a 334 MW High Efficiency Combined Heat and Power (CHP/High Efficiency CHP) plant. Power production was enhanced with the initiation of commercial operation of a new 444.48 MW Combined Cycle Thermal Power Plant (CCGT) in the same area, in June 2011.

The total volume of water withdrawn required for the Group's activities in 2015 stood at 164.8 million m^3, down by 0.8% from 2014. This reduction is mainly due to the restriction by 2 million m^3 of the volume of seawater withdrawn for use in the cooling systems of the Group's heavy industry plants. More specific, regarding the seawater used in the cooling systems of the Combined Heat and Power (CH) plant of ALUMINIUM OF GREECE, in addition to the strict compliance with the relevant provisions of the laws determining the framework for preventing any environmental impact, the company commissions, on an annual basis, an authoritative organisation (Hellenic Centre for Marine Research - HCMR) to conduct of a research study to monitor the status of living organisms (benthic biocoenoses, with emphasis on thermophilic species) on the Antikyra Gulf seabed.

Table 1.) Characteristics of the cooling sea water based on the Sustainability Report 2016 of MYTILINEOS Group

Category	Quantity	Destination	Quality of water discharges
From the cooling process of the combined Heat and Power (CHP) plant	124 044 607 m^3/year	Discharge to the sea	pH: 8-8,2 Temperature: 22,3 ∘C
Wastewater including rainwater	539 220 m^3/year	Discharge to the sea	pH: 7,87 BOD5: 2,6 mg/L COD: <7 mg/L Total Solids: 681,67 mg/L Total Suspended Solids: <25 mg/L Sulphides: <0,05 mg/L

Table 2.) Evolution of the used cooling water based on the Sustainability Report 2016 of MYTILINEOS Group

Surface water (m^3)	2014	2015	2016
Volume of seawater used in the cooling systems of the Combined Heat and Power (CHP) plant	161 733 577	159 609 769	124 044 607

1.2.1.) Extraction of alumina from the bauxite

Pure alumina (aluminum oxide) is extracted from bauxite by the Bayer process. In the Bayer process bauxite received from the mines is crushed, usually by a hammer mill to small particles and well blended. Lime (CaO) is added to assist in the extraction of alumina, to scavenge impurities, and later to enhance clarification. This mixture then flows to agitated storage tanks and is metered into high-temperature (~255°C) sodium hydroxide digesters (NaOH), where alumina is extracted from the bauxite as sodium aluminate (NaAlO2). Pure alumina is then precipitated (by lowering temperature to 50-70°C) from the solution as a hydroxide [Al(OH)$_3$], filtered, washed, and then calcined to pure alumina (Al$_2$O$_3$) at 1100–1200°C.

This procedure leaves behind the impurities as an insoluble residue, mainly consisting of hematite (Fe$_2$O$_3$), titania (TiO$_2$), and silica (SiO$_2$). For the production of one tone of alumina two tons of bauxite are needed. The "Aluminum of Greece S. A." produces more than 750,000 tones alumina yearly. The extraction of alumina from the bauxite is supported from two smaller industrial units:

a. The unit producing CaO (needed by the extraction procedure) from limestones coming from the geological formations exposed near the industrial field.

b. A unit producing thermal energy, needed also for the procedure. Using as energy resource imported crude oil.

1.2.3.) Extraction of aluminum metal from the alumina

Aluminum metal is extracted from the alumina electrolytically by the Hall–Heroult process. In this process, the purified alumina is dissolved in an electrolyte consisting mainly of molten at ~960°C cryolite (NaF/AlF$_3$). Consumable carbon anodes are employed, producing carbon dioxide and carbon monoxide, which escape from the cell while the molten aluminum accumulates at the cathodic bottom and is siphoned out periodically. The aluminum produced is normally 99.6–99.9% pure. The typical impurities are iron, silicon, titanium, vanadium, gallium, and manganese, coming from the anode but also from impurities in the alumina. The "Aluminum of Greece S. A. [AtE]" produces approximately 170,000 tones aluminum metal yearly.

2.) Data and methods

The methodology for the present work is discussed in two parts: First, the pre-processing phase in which all satellite images were calibrated, masked from land and then corrected from atmospheric effects. After that, two different methods have been used in order to assess the seawater surface temperature (SST) and to evaluate the performance of satellite in determining Chl-a concentrations.

2.1.) Satellite data and sea surface temperature estimation

All materials with a temperature above 0 K emit radiation, and as described by Wien's Displacement Law, the hotter the object, the shorter the wavelength of its emitted radiation. For example, the sun's temperature is approximately 6000 K, and the sun emits its peak radiation in the visible part of the electromagnetic spectrum (0.4–0.8μm) to which the human eye is adapted. Remote sensing in the region of visible, near infrared (NIR) and midinfrared radiation (<3μm) utilises reflected radiation. In contrast, the earth's ambient temperature is ~300 K and its peak radiation is emitted at the longer wavelength of 9.7μm. Thermal remote sensing captures radiation emitted in these longer wavelengths (3–1000μm). As thermal infrared (TIR) observations are strongly affected by radiation absorbed and emitted from water vapour, TIR applications focus on the 8–14μm region of the electromagnetic spectrum where atmospheric interference and contamination by solar radiation (in the 3–5μm region) is minimized (Handcock et al., 2012).

2.1.1.) Landsat satellite sensors

The **Landsat Thematic Mapper (TM)** sensor was carried on Landsat 4 and Landsat 5, and its images consist of six spectral bands with a spatial resolution of 30 meters for Bands 1-5 and 7, and one thermal band (Band 6). The approximate scene size is 170 km north-south by 183 km east-west (Barsi et al., 2014).

Table 3.) Characteristics of the Landsat TM sensor systems (USGS)

Bands	Wavelength (µm)	Resolution (m)
Band 1 - Blue	0.45-0.52	30
Band 2 - Green	0.52-0.60	30
Band 3 - Red	0.63-0.69	30
Band 4 - Near Infrared (NIR)	0.76-0.90	30
Band 5 - Shortwave Infrared (SWIR) 1	1.55-1.75	30
Band 6 - Thermal	10.40-12.50	120* (30)
Band 7 - Shortwave Infrared (SWIR) 2	2.08-2.35	30

The **Landsat Enhanced Thematic Mapper Plus (ETM+)** sensor is carried on Landsat 7, and images consist of seven spectral bands with a spatial resolution of 30 meters for Bands 1-5, and 7. The resolution for Band 8 (panchromatic) is 15 meters. All bands can collect one of two gain settings (low or high) for increased radiometric sensitivity and dynamic range, while Band 6 collects both low and high gain (Bands 61 and 62, respectively) for all scenes. (Barsi et al., 2014).

Table 4.) Characteristics of the Landsat ETM+ sensor systems (USGS)

Bands	Wavelength (µm)	Resolution (m)
Band 1 - Blue	0.45-0.52	30
Band 2 - Green	0.52-0.60	30
Band 3 - Red	0.63-0.69	30
Band 4 - Near Infrared (NIR)	0.77-0.90	30
Band 5 - Shortwave Infrared (SWIR) 1	1.55-1.75	30
Band 6 - Thermal	10.40-12.50	60 * (30)
Band 7 - Shortwave Infrared (SWIR) 2	2.09-2.35	30
Band 8 - Panchromatic	.52-.90	15

Landsat 8 Operational Land Imager (OLI) and Thermal Infrared Sensor (TIRS) images consist of nine spectral bands with a spatial resolution of 30 meters for Bands 1 to 7 and 9. The ultra blue Band 1 is useful for coastal and aerosol studies (Barsi et al., 2014) while Band 9 is used usually for cirrus cloud detection. It is important to mention that Thermal bands 10 and 11 provide more accurate surface temperatures. The approximate scene size is 170 km north-south by 183 km east-west.

Table 5.) Characteristics of the Landsat OLI and TIRS sensor systems (USGS)

Bands	Wavelength (μm)	Resolution (m)
Band 1 - Ultra Blue (coastal/aerosol)	0.435 - 0.451	30
Band 2 - Blue	0.452 - 0.512	30
Band 3 - Green	0.533 - 0.590	30
Band 4 - Red	0.636 - 0.673	30
Band 5 - Near Infrared (NIR)	0.851 - 0.879	30
Band 6 - Shortwave Infrared (SWIR) 1	1.566 - 1.651	30
Band 7 - Shortwave Infrared (SWIR) 2	2.107 - 2.294	30
Band 8 - Panchromatic	0.503 - 0.676	15
Band 9 - Cirrus	1.363 - 1.384	30
Band 10 - Thermal Infrared (TIRS) 1	10.60 - 11.19	100 * (30)
Band 11 - Thermal Infrared (TIRS) 2	11.50 - 12.51	100 * (30)

2.1.2.) Remote sensing

Remote Sensing and GIS are powerful tools which provide solutions for water resources management problems. Especially, thermal remote sensing is based on recording the electromagnetic radiation in the thermal infrared region (TIR) emitted by surface objects as a function of their temperature in two windows: 3.5–5 μm and 8.0–14.0 μm. Therefore, thermal images can be acquired during both day and night (UNESCO, 2007). Thermal infrared remote sensing (TIR) technique is a useful approach to monitor change of water temperature (UNESCO, 1982). TIR Bands of Landsat-5 Thematic Mapper (TM), Landsat-7 Enhanced Thematic Mapper (ETM) has wide range of electromagnetic wavelength band, including visible, infrared and thermal bands. Its thermal bands can detect thermal radiation released from objects on the earth surface (Xing and Chen, 2006). TIR data can aid identifying a severe environmental phenomenon: thermal pollution resulting from power planet and industry discharges of water used in cooling processes.

This study used for the temperature estimation the thermal infrared (TIR) remote sensing, from the satellite images of Landsat Thematic Mapper (TM) scenes from Landsat 5, and the Landsat Enhanced Thematic Mapper (ETM+) of Landsat 7. The data were acquired for all available TM images with less than 20% cloud cover from 1960 to 2011 and for one ETM+ images per month until 10.12.2016.
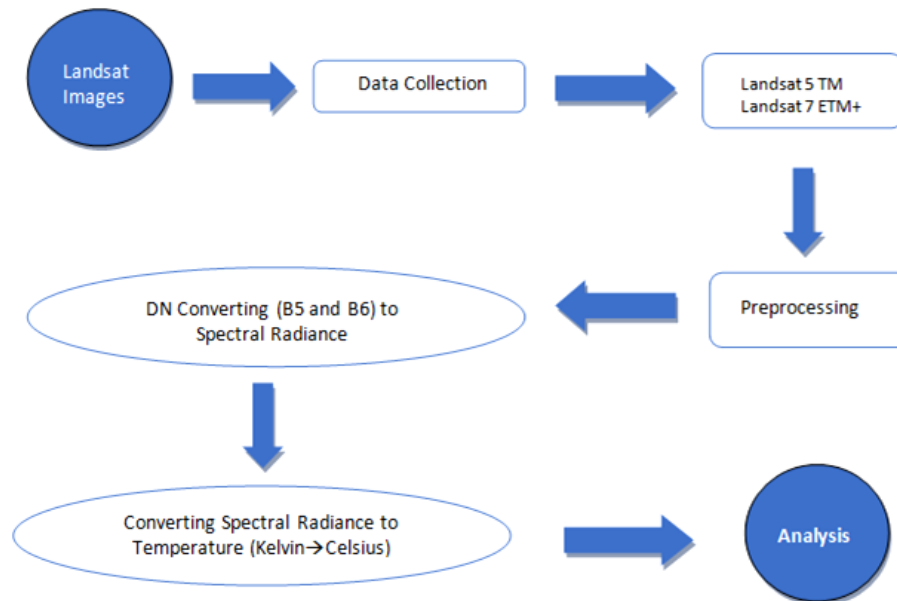
Fig.7.) Major steps of the temperature estimation based on Landsat data

2.1.3.) Preprocessing

The raw digital numbers of a Landsat image are not only dependent on the reflectance characteristics of the specific scene, but also contain noise and digital number value offsets that are a result of the viewing geometry of the satellite, the angle of the sun's incoming radiation, atmospheric depth due to viewing angle, and the design characteristics of the sensor. For this reason, the data must first be converted to radiance, which removes the voltage bias and gains from the satellite sensor. The radiance values are then further converted to at-satellite reflectance. This conversion accounts for the varying sun angle due to differences in latitude, season, and time of day, and the variation in the distance between the Earth and Sun. The objective of atmospheric correction is to retrieve the actual "clear sky" surface reflectance from remotely sensed imagery by removing the specific weather related atmospheric noise from a specific scene. Atmospheric correction has been shown to significantly improve the accuracy of image classification in some instances, but decrease the accuracy in other instances (Loveland and Dwyer, 2012)

In this study, 58 Landsat L1T images were used as they are more precisely registered than the Level 1 Systematic (corrected) (L1G) images. These images includes radiometric, geometric, and precision correction, and uses a DEM to correct parallax error due to local topographic relief (Markham and Helder, 2012).

In order to decrease the image processing time, the whole image scenes were detruncated, and the image part covering the study area was extracted (region of interest, ROI). The water-land boundary was identified by the band-5 images, as water has strong absorption at SWIR band. The counts of band 6 data were transferred to radiance ($Wm^{-2}nm^{-1}Sr^{-1}$) value by

ENVI5.1 software, and then the radiance data were used for calculation of water surface temperature.
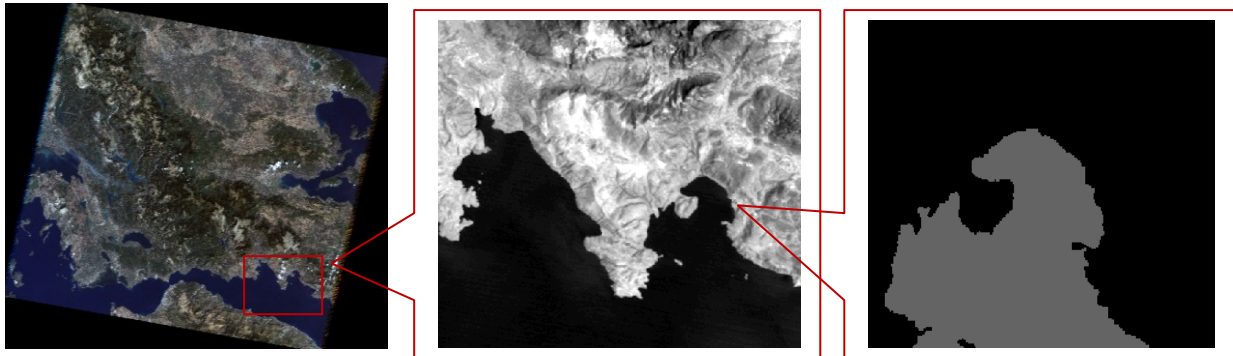

Fig. 8.) Processing steps from right to left: region of interest--> land mask--> band 6 radiance with mask

2.1.4.) Converting radiance into Sea Surface Temperature

The first step of the algorithm is retrieving the top of atmospheric (TOA) spectral radiance (L_λ) (Barsi et al., 2014):

$$L_\lambda = M_L * Q_{cal} + A_L - O_i \qquad (1)$$

M_L : the band-specific multiplicative rescaling factor
Q_{cal} : the Band 6 image
A_L: the band-specific additive rescaling factor
O_i: the correction for Band 6

After the digital numbers (DN) are converted to reflection, the TIRS band data should be converted from spectral radiance to brightness temperature (BT) using the thermal constants provided in the metadata file. The following equation (Xu and Chan, 2004) is used in the tool's algorithm to convert reflectance to temperature:

$$BT = K_2 \ln\left[(K_1/L_\lambda) + 1\right] - 273.15 \qquad (2)$$

where K_1 and K_2 stand for the band-specific thermal conversion constants from the metadata. For obtaining the results in Celsius, the radiant temperature is revised by adding the absolute zero (approx. −273.15° C).

Furthermore the emissivity has to be corrected since the LSE is a proportionality factor that scales blackbody radiance (Planck's law) to predict emitted radiance, and it is the efficiency of transmitting thermal energy across the surface into the atmosphere.

$$\varepsilon_\lambda = \varepsilon_{V\lambda}P_V + \varepsilon_{s\lambda}(1-P_V) + C_\lambda \qquad (3)$$

where ε_V and ε_s are the vegetation and soil emissivities, respectively, and C_λ represents the surface roughness (C_λ = 0 for homogenous and flat surfaces) taken as a constant value of 0.005. The condition can be represented with the following formula and the emissivity constant values:

$$\varepsilon_\lambda \;=\; \begin{cases} \varepsilon_{s\lambda}, & \text{NDVI} < \text{NDVI}_s, \\ \varepsilon_{v\lambda} P_v + \varepsilon_{s\lambda}(1 - P_v) + C, & \text{NDVI}_s \le \text{NDVI} \le \text{NDVI}_v, \\ \varepsilon_{s\lambda} + C, & \text{NDVI} > \text{NDVI}_v. \end{cases} \qquad (4)$$

$$\text{NDVI} = \text{NIR (band 5)} - R\text{ (band 4)} \,/\, \text{NIR (band 5)} + R\text{ (band 4)} \qquad (5)$$

NIR: the near-infrared band
R: the red band.

The last step of retrieving the SST or the emissivity-corrected surface temperature SST is computed based on the methodology of Stathopoulou and Cartalis (2007):

$$\text{SST} = \text{BT} \,/\, \{1 + [(\lambda \text{BT}/\rho)\ln \varepsilon_\lambda]\} \qquad (6)$$

λ: the wavelength of emitted radiance
ε_λ: the emissivity

$$\rho = h\,c\,\sigma = 1.438 \times 10^{-2}\,\text{m K} \qquad (7)$$

σ: the Boltzmann constant ($1.38 \times 10{-}23$ J/K)
h: Planck's constant ($6.626 \times 10{-}34$ J s)
c: the velocity of light (2.998×108 m/s)

2.1.5.) Statistical Analysis

In order to investigate if the aluminum plant significantly affects the sea surface temperature of Antikyra Bay, we compared the SST fields of the Bay with the SST fields of the neighbouring Itea bay of very similar morphological and hydrographic characteristics. Assuming the Itea Bay being the "model", or "estimated" condition, and the Antikyra Bay being the "observed" or "measured", comparison between the area of Antikyra Bay and the neighbour bay, named Itea Bay, was performed using the following statistic metrics: the root mean squared error (RMSE), t-test, mean absolute percentage error (MAPE), mean normalized bias (MNB) and determination coefficient (R^2):

$$\text{RMSE} = \sqrt{\frac{1}{n} \sum_{i=1}^{n} \left(x_i^{\text{estimated}} - x_i^{\text{measured}} \right)^2} \qquad (12)$$

$$\text{MAPE}=\frac{\Sigma_{i=1}^{n}\left(\left|\frac{x_i^{estimated}-x_i^{measured}}{x_i^{measured}}\right|\right)}{n} \tag{13}$$

$$\text{bias}=\frac{1}{n}\Sigma_{i=1}^{n}(x_i^{estimated}-x_i^{measured}) \tag{14}$$

$$\text{NSE}=1-\frac{\Sigma_{i=1}^{n}\left(x_i^{measured}-x_i^{estimated}\right)^2}{\Sigma_{i=1}^{n}(x_i^{measured}-mean(x_i^{measured}))^2} \tag{15}$$

Furthermore, in order to quantify the degree of correspondence between the two time series, a Taylor diagram has been used. This summarizing performance diagram, based on the methodology of Taylor (2001), assesses the similarity of the data values with the relation of three statistics: the Pearson correlation coefficient, the root-mean-square error (RMSE) error, and the standard deviation. Mathematically, the three statistics displayed on a Taylor diagram are related by the following formula:

$$E'^2=2\sigma_r^2 + 2\sigma_t^2 - 2\sigma_r\sigma_t\rho \tag{16}$$

ρ: the correlation coefficient between the two time series
E': the centered RMS difference between the fields
σ_r, σ_t: the variances of the reference and test fields, respectively.

2.2.) Satellite data and chlorophyll-a concentration estimation

Chlorophyll-a (Chl-a) concentration can be used as a direct indicator of the ecological state of a water body. For example, an algal bloom can degrade water quality in rivers, lakes, and reservoirs, and Chl-a concentration has been shown useful as an indicator for measuring the abundance and variety of phytoplankton and/or the algal biomass (Boyer et al., 2009). Since the 1990s, the development of satellite technology, greater understanding of the spectral signature of water quality parameters, and the development of mathematical models have led to semi-empirical methods becoming the principal means with which to monitor water quality remotely. Studies on water environmental protection and the monitoring of water quality have become increasingly important because of the severe environmental problems affecting surface water (Wang et al., 2015). Point-to-surface and static-to-dynamic monitoring of water quality are required urgently. However, it is difficult to perform long-term monitoring over large areas. Research based on remote sensing techniques and the spectral characteristics of water is extremely valuable for large-scale monitoring of water quality, especially when traditional water sampling analysis methods are restricted by factors such as labor and material costs, and climatological and hydrological conditions. Inversion of water quality parameters using remote sensing technology can improve the monitoring of surface water quality and derive dynamic water quality information in real-time. Thus, this technique represents an important complement to regular water quality monitoring, and it can provide a robust scientific basis for governmental decision-making in

relation to the ecological economic zone. Chl-a concentration has been used as an important index to reflect water quality conditions (Le et al., 2013). Accurate information on the spatiotemporal variation of Chl-a concentration can contribute to improved understanding of water quality status and assist water-resource management. Traditional methods used to monitor Chl-a concentration, e.g., spectrophotometry, have many limitations: high cost, complex method of operation, restriction of observations to specific regions and specific times, and long monitoring periods. The lack of in situ real-time monitoring data on the quality and optical properties of inland water bodies renders it difficult to determine the spatiotemporal variation of Chl-a concentration. Satellite remote sensing technology has shown great potential in providing spatial distribution patterns of Chl-a (Sun et al., 2014). The application of such technology can be cost effective, shorten the period of observation, and increase the temporal frequency of sampling. Furthermore, in conjunction with an accurate and efficient inversion model, the technology can realize real-time, synchronous, large-area, and continuous monitoring of Chl-a concentration in a target area (Pan et al., 2012). Thus, remote sensing techniques are able to overcome the shortcomings of traditional observational methods. In particular, improvements of the geometry and the spectral resolution associated with remote sensing technology have presented new possibilities for the evaluation of water resources via the monitoring of Chl-a concentration.

Numerous studies suggest that chlorophyll-a in waters can be measured using Landsat imagery (Keiner and Yan, 1998; Giardino, 2001; Zhang et al., 2002; Erkkilä and Kalliola, 2004; Hellweger, 2004; Sudheer et al., 2006, Kabbara et al., 2008; Kulkarni, 2011; Nazeer and Ncichol, 2016). Han and Jordan (2005) discovered strong correlation between the ratio of Band1/Band3 and in situ chlorophyll-a concentration in the Pensacola Bay on the Gulf of Mexico. Kabbara et al. (2008) reported that there were significant correlations (R^2 = 0.719 - 0.7234) between the surface chlorophyll-a concentrations and spectral indices based on the combination of blue/green or blue/red band. Lim et al. (2009) revealed the correlation coefficient of 0.8259 between the predicted and the measured chlorophyll-a values. Kulkarni (2011) stated that chlorophyll-a could be retrieved using models based on the red or green band and the model with the green band value showed the highest correlation (R^2=0.864) with chlorophyll-a content in waters. Torbick et al. (2013) concluded that there was a strong correlation (R^2=0.65-0.81) between band ratio radiance and water quality indicators including Sechhi depth (SD), chlorophyll-a, green biovolume, total phosphorus (TP), and total nitrogen (TN). The correlation coefficient of green and blue ratio and chlorophyll-a (0.89) was obtained by Nazeer and Nichol (2016). These results suggested that chlorophyll-a in waters can be effectively retrieved from the Landsat imagery using appropriate algorithms.

2.2.1.) Preprocessing
For the part of the chlorophyll-a concentration modeling Landsat OLI and TIRS images from Landsat 8 were used. The data were acquired for images with less than 20% cloud cover for

the dates with available in-situ chlorophyll-a data from April 2014 to October 2015. The only bands imported into ENVI were band 1 (coastal blue band), band 2 (blue band), band 3 (green band), band 4 (red band) and band 5 (near infra-red band). The preprocessing part for the Landsat 8 images was based on the Spectral Radiance Scaling Method as shown below.

As outlined in the online Landsat User's Guide Chapter 11 there is a standard procedure to convert Landsat radiance values into reflectance (at satellite) values. To do this a simple formula can be used:

$$R_{sesnor} = \frac{\pi * L * d^2}{ESUNi * \cos(z)} \qquad (17)$$

$$\pi = 3.14159$$

ESUN$_i$: the mean solar exoatmospheric irradiance of each band
z: the solar zenith angle (zenith angle = 90 – solar elevation angle) from the header file
d: the earth-sun distance, by the follow equation (Eva and Lambin, 1998):

$$d = (1-0.01672*\cos(radians(0.9856*(Julian\ Day-4)))) \qquad (18)$$

L: the spectral radiance at the sensor's aperture (W/(m²*ster*μm) by the equation:

$$L = ((Lmax\lambda - Lmin\lambda)/(Qcalmax-Qcalmin)) * (Qcal-Qcalmin) + Lmin\lambda \qquad (19)$$

Qcal: the quantized calibrated pixel value (DN)
Lminλ: the spectral radiance that is scaled to Qcalmin (W/(m^2*ster*μm)
Lmaxλ: the spectral radiance that is scaled to Qcalmax (W/(m^2*ster*μm)
Qcalmin: the minimum quantized calibrated pixel value (DN)
Qcalmax: the maximum quantized calibrated pixel value (DN)

After the atmospheric correction, band ratios for different band combinations such as b2/b1 were calculated for five bands from band 1 to band 5 using ENVI for each Landsat OLI image. Two Middle infrared bands (OLI6 and OLI7) were not included in the computation and later analysis due to their lower sensitivity to chlorophyll-*a* concentration in water. After the necessary analysis the landsat data were correlated with in situ measurements of chlorophyll-a values in certain sampling stations. Several models were used to examine these relationships which included linear, exponential, and log transformations.
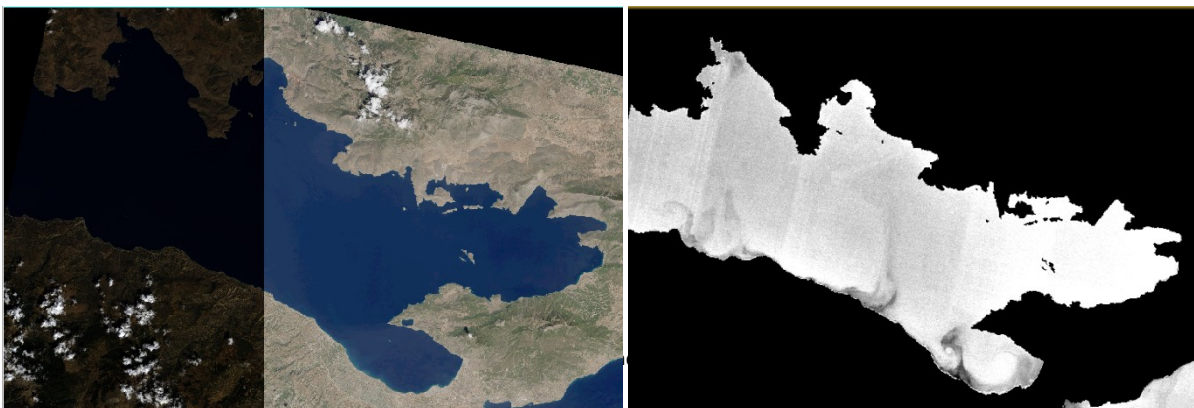
Fig.9.) Preprocessing workflow: Radiometric and atmospheric correction, land masking

2.2.1.) Model selection

The Landsat data, after their calibration, atmospheric correction, and transformation, were correlated with in situ measurements of chlorophyll-a values in certain sampling stations. Chlorophyll-*a* samples have been collected by the Hellenic Centre for Marine Research at 4 different stations, in Antikyra Bay from April 2014 until October 2015. Satellite images of Landsat 8 of the same area and the same dates were used in order to statistically correlate the *in-situ* measurements with various combinations of Landsat bands in order to quantify algorithms that best describe this relationship and calculate accurately the concentration of chlorophyll-*a*. The algorithms were applied to other satellite images of different dates but with available in-situ chl-*a* data, in order to validate the results. Satellite derived chlorophyll-*a* values were compared to *in-situ* chlorophyll-*a* values originated from other past scientific studies. The initial results confirmed the suitability of the method for assessing the concentration of chlorophyll-*a* in the Gulf of Corinth with relative accuracy when no field data are available.

The selection of the best applicable model was based on the value of the correlation of determination between the reflectance and the values of chlorophyll-*a*. The best predictive model (developed based on field sampling of 5 September 2013 and 6 and 7 November 2013 and satellite images of 5/9/2013 and 7/11/2013 were applied to the Landsat imageries of 26/4/2014, 24/10/2014, 3/12/2014, 16/4/2015, and 6/10/2015 in order to assess and validate its efficiency by comparing them with the *in situ* measurements from the specific study area and for the same dates.

2.2.2.) Model Validation

The algorithms performance was evaluated using the following statistic metrics: normalized root mean squared error (NRMSE), the root mean squared error (RMSE), mean absolute percentage error (MAPE), bias, mean normalized bias (MNB) and determination coefficient (R^2):

$$NRMSE = \frac{RMSE}{(x_{max}^{measured} - x_{min}^{measured})} \tag{20}$$

$$RMSE = \sqrt{\frac{1}{n} \sum_{i=1}^{n} \left(x_i^{estimated} - x_i^{measured}\right)^2} \tag{21}$$

$$MAPE = \frac{\sum_{i=1}^{n} \left(\left|\frac{x_i^{estimated} - x_i^{measured}}{x_i^{measured}}\right|\right)}{n} \tag{22}$$

$$bias = \frac{1}{n} \sum_{i=1}^{n} (x_i^{estimated} - x_i^{measured}) \tag{23}$$

$$NSE = 1 - \frac{\sum_{i=1}^{n}\left(x_i^{measured} - x_i^{estimated}\right)^2}{\sum_{i=1}^{n}(x_i^{measured} - mean(x_i^{measured}))^2} \tag{24}$$

In addition, a Taylor diagram (Taylor, 2001) was used, since they provide a way of graphically summarizing how closely a pattern matches observations, as mentioned in (2.1.5.). The similarity between the two datasets is quantified in terms of their correlation, their centered root-mean-square difference and the amplitude of their variations (represented by their standard deviations).

2.3.) Chlorophyll-a in-situ concentrations

Data for this study were obtained from the National Monitoring Project of Greece, assigned to the Hellenic Centre for Marine Research by the Hellenic Ministry of Environment, Energy and Climate Change, Special Secretary of Water and was kindly provided by Dr. Asimakopoulou from the Hellenic Centre for Marine Research. The data set used originated from sampling of 4 stations (table 6) of the national monitoring network designed for the implementation of the WFD in the coastal waters. This first sampling cruise of the monitoring network, during which the data presented were collected, was conducted in 5/9/2013, 7/11/2013, 26/4/2014, 24/10/2014, 3/12/2014, 16/4/2015, 6/10/2015 in 4 stations by the R/V PHILIA of HCMR ownership.

Table 6.) Sampling stations with coordinates

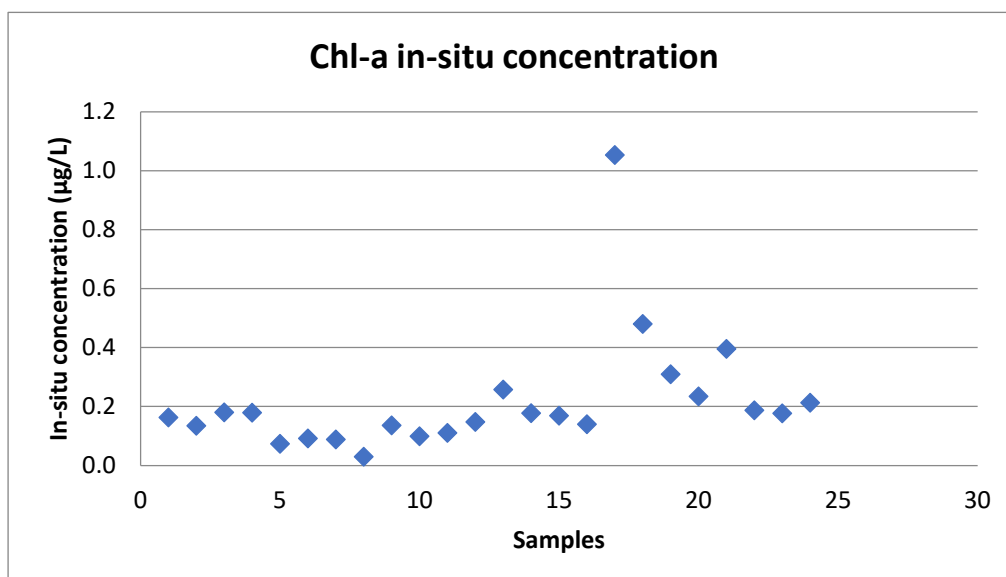| Station	Latitude	Longitude
A1	38°22,550	22°40,673
A2	38°20,831	22°40,624
A3	38°21,128	22°40,814
A4	38°20,666	22°41,138

Fig.10.) In-situ concentrations of the sampling stations in Antikyra Bay

The biomass of the phytoplankton (as chlorophyll-a) constitutes an important ecological quality descriptor for the coastal environment. The phytoplankton biomass is most frequently measured as the concentration of chlorophyll-a at discrete depths in the euphotic portion of the water column and is measured in the seawater samples collected also for the physicochemical parameters from the discrete standard depths of 2m, 10m, 20m, 50m and the bottom layer.

2.4.) NCEP/NCAR Air-Sea flux data

Air-sea flux data have been derived from the National Center for Atmospheric Prediction (NCEP) and the National Center for Atmospheric Research (NCAR) daily reanalysis (http://www.esrl.noaa.gov/psd/) and were used to examine time-series of air-sea fluxes and heat loss using Matlab R2013a. The data assimilation system uses a 3D-variational analysis scheme, with 28 sigma levels in the vertical and a triangular truncation of 62 waves which corresponds to a horizontal resolution of approximately 200 km (Kalnay et. al, 1996).

In order to analyze how the atmosphere influences the SST variation, the correlation of the net air-sea heat flux and the different radiations and heat losses with sea surface temperature were estimated.

According to Rahul and Gnanaseelan (2013) the net heat flux into the ocean is a sum of different heat exchange processes at ocean surface, which includes heating due to short-wave radiation (SW), outgoing long-wave radiation (LW), sensible heat flux (SH), and latent heat flux (LH):

$$Qnet = SW - LW - SH - LH \qquad\qquad (25)$$

It is noteworthy that the first component (SW) is the contributor to the heat gain of ocean, and all the other processes lead to heat loss, except for SH, which depends on air–sea temperature difference. The latent heat loss, the heat required for the evaporation of surface water, is the major contributor to oceanic heat loss, followed by radiative cooling due to net outgoing long-wave radiation. The SH contribution to the net heat flux into the ocean is relatively small. The latent heat loss is dependent on three factors, namely, SST, air humidity, and surface winds. The radiative cooling is a function of SST, and the incoming long-wave radiation depends upon many factors such as atmospheric temperature, water vapor, and greenhouse gas concentrations.

2.4.1.) Atmosphere influences assessment

In order to analyze the atmosphere influences for the sea surface temperature (SST) variation, the Frankignoul method have been used (Frakignoul et al., 1998). This method is

based on the fact that the surface heat flux contributes to generate SST anomalies but it also affect their evolution after they have been generated, thereby acting as a feedback. As showed by Frakignoul et al. (1998) the surface heat flux anomalies can be decomposed as:

$$Q_{surf}(\tau) = q(\tau)\text{-}\alpha\text{*}SST \qquad\qquad (26)$$

q: independent of the SST anomalies
-α*SST: the Q_{surf} induced by the SST anomalies

From equation (26), the cross-covariance between Qsurf and SST can be computed by:
$$Cov_{Qsurf/SST}(\tau) = Cov_{q/SST}(\tau) - \alpha\, Cov_{SST/SST}(\tau) \qquad\qquad (27)$$

Since $Cov_{q/SST}(\tau)$ vanishes at large negative lag (τ>1 month) the feedback of the surface heat flux can be estimated using the cross-covariance between SST and Q_{surf}, divided by the autocovariance of the SST:

$$\alpha = -\frac{Cov[Qsurf(-1), SSTf(0)]}{Cov[SST(-1), SSTf(0)]} \qquad\qquad (28)$$

3.) Results

The remote sensing based analysis described in section (2) led to three main results:

a) the monitoring of the temporal evolution of the sea surface temperature in Antikyra Bay and Itea Bay, which made it possible to estimate the thermal effluent of the aluminum plant in Antikyra Bay.

b) the development of a local high resolution analysis chlorophyll-a concentration monitoring algorithm for the Gulf of Corinth.

c) the assessment of the atmosphere influences on the sea surface temperature variation

3.1.) Sea surface temperature

After the preprocessing and the necessary analysis, time series for temperature data in the area of the Aluminum plant in Antikyra Bay and for a control area in the Itea Bay (Figure 11.) were compared (Figure 12.).

Figure 11.) Landsat 7 image indentifying the (red) study area and the (white) control area

For this two areas temperature time series from late 2009 up to early 2017 were extracted in order to compare them and to indentify whether the hot cooling water from the aluminum plant, which where establish in 2010, does have impact on the local area or not. From the graph below although it seems that the two areas doesn't differ much. In order to investigate this further statistical analysis are presented in (3.1.1.).
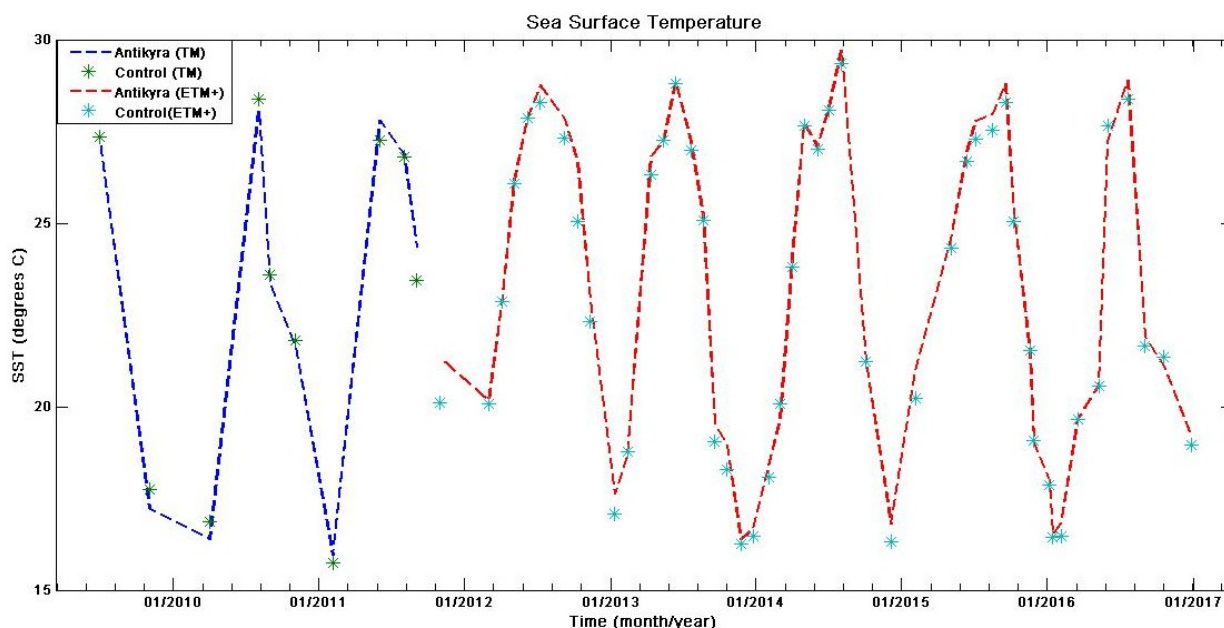
Figure 12.) Time series of sea surface temperature for the area of Antikyra Bay (dotted line) and the control area of Itea Bay (points) based on Landsat 5 (TM) and Landsat 7 (ETM+) imagery

Also, it can be seen that the Sea Surface Temperature in the area of the aluminum plant doesn't differ much from the control dataset of Itea bay. Furthermore, at least the optical analysis didn't reveal any thermal plume in the area of the aluminum plant. In order to compare the two time series further, statistical indexes have been used and are presented below in section 3.1.2.).

3.1.1.) Seasonal sea surface temperature variation

The seasonal SST values, estimated by averaging the three successive months associated with the four seasons in oceanography, i.e., January-February-March for winter, April-May-June for spring, July-August-September for summer and October-November-December for autumn, seemed to show an annual pattern with a normal shape during the year. The maximum temperature was found during summer 2014 (29.70 °C) and the minimum (16.38 °C) in winter 2011.

Table 7.) Mean seasonal sea surface temperature for 2010-2016

Season	2010	2011	2012	2013	2014	2015	2016	Mean
Winter	18.026	16.934	19.021	17.563	17.824	17.901	18.423	17.956
Spring	21.584	no data	20.809	19.843	20.354	21.325	20.023	20.656
Summer	25.407	24.975	24.714	25.123	26.465	24.237	25.209	25.161
Autumn	21.743	20.988	21.924	21.221	20.853	19.022	21.589	21.048

The time series analysis revealed the presence of a strong seasonal signal characterized by two main seasonal extremes, winter and summer (Fig.13.). The transition between the winter and the summer occurs usually rapidly in May and October.
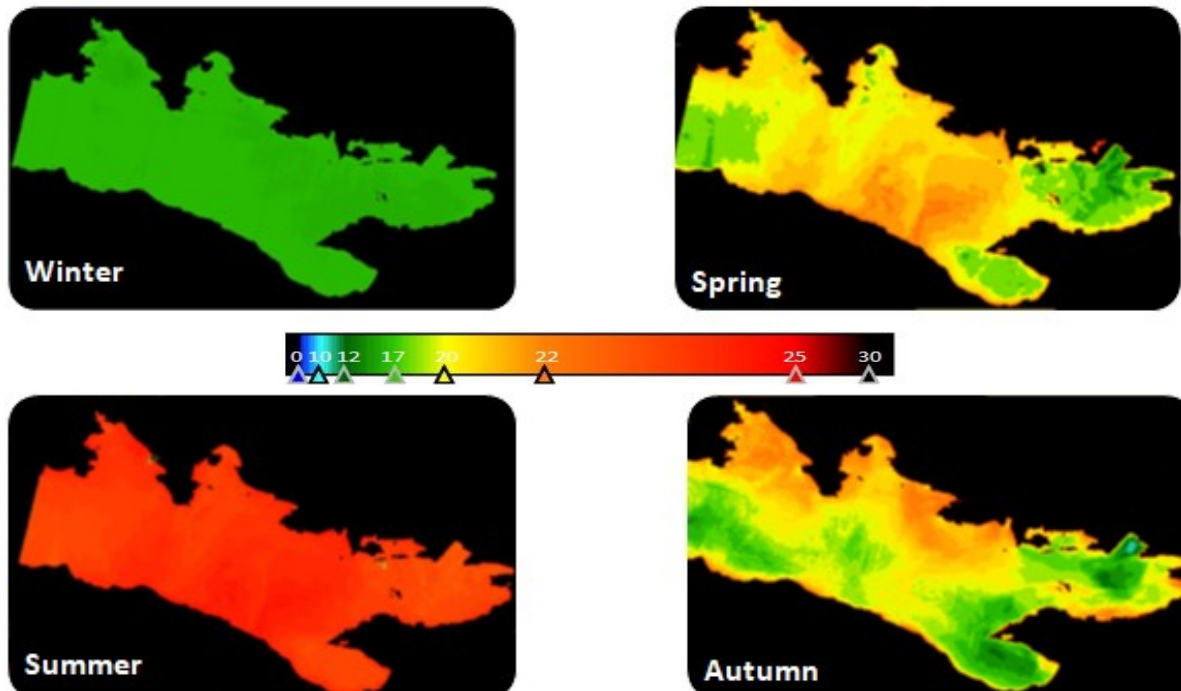
Fig.13.) Seasonly mean images of SST distribution for 2010-2016 (°C). The mean SST values were estimated by averaging the images of Landsat satellite images at 30m resolution

3.1.2.) Statistical Analysis

The statistical indices based on the equations (12) – (16) for the dataset of the sea surface temperature of Antikyra Bay and Itea Bay revealed strong correlation and statistically important similarity. Therefore it can be assumed that there is no detectable temperature increase in the area of the aluminum plant. Some possible explanations are discussed in the followed section (4).
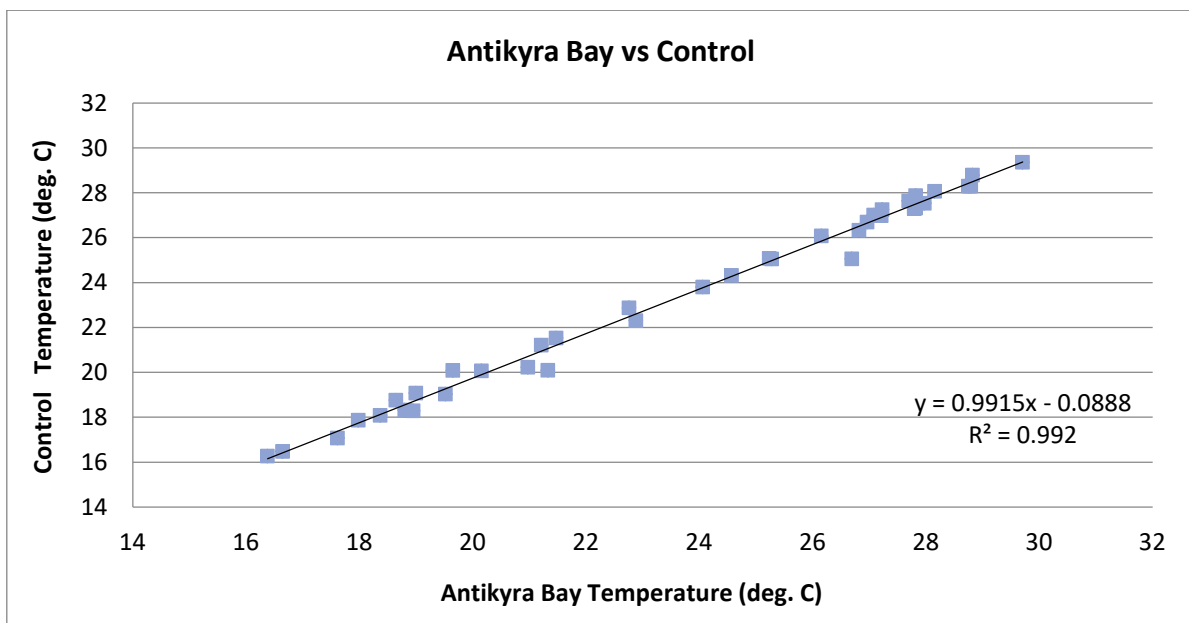

Fig.14.) Scatter plot of the compared SST datasets indicating their relation and determination coefficient (R[2])

Below are presented the statistic metrics mentioned in the methodology based on the equations (20)-(24) and their normalized indexes: root mean squared distance (RMSD), normalized root mean squared error (NRMSE), mean absolute percentage error (MAPE), PBIAS, NSE, mNSE, RSR correlation coefficient (Correl) and determination coefficient (R^2):

Table 8.) Statistical indices of the two temperature datasets

Statistic index	Value	Goodness of fit
RMSD	**0.17**	Perfect=0
NRMSE	**0.04**	Perfect=0
MAPE	**0.02**	Perfect=0
PBIAS	**1.04**	<25%
NSE	**0.98**	>0.5
mNSE	**0.91**	>0.5
RSR	**0.13**	<0.70
Correl	**0.98**	Exact=1
R^2	**0.99**	Exact=1

Furthermore, a Taylor diagram is shown below for more descriptive presentation of the statistic analysis:

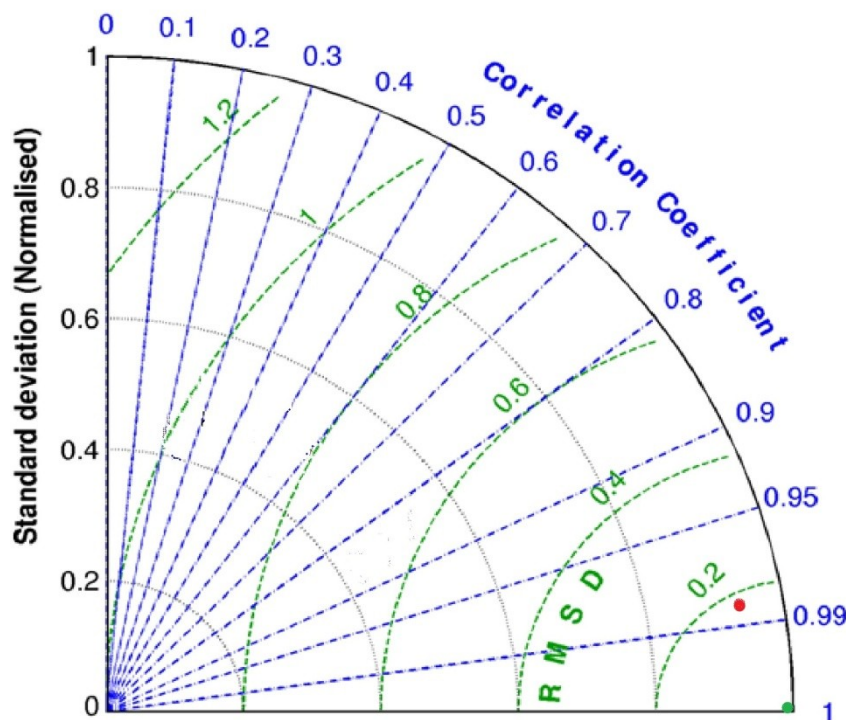Fig.15.) Taylor diagram displaying the statistical comparison with sea surface temperature in Itea Bay (control:green dot) and Antikyra Bay (red dot)

As it can be seen in the Taylor diagram three statistics are plotted: the Pearson correlation coefficient (gauging similarity in pattern between the simulated and observed fields) is related to the azimuthal angle (blue contours); the centered RMS distance in the simulated

field is proportional to the distance from the point on the x-axis identified as "observed" (green contours); and the standard deviation of the simulated pattern is proportional to the radial distance from the origin (black contours). It is evident from this diagram that the Pearson correlation coefficient is about 0.98, the RMSD error is about 0.17 and the standard deviation is about 0.14 °C.

3.2.) Chlorophyll-a concentration

In this study, the coefficient of determination (R^2) among in-situ Chl-a concentrations and reflectance values from 51 different empirical models based on single bands, band ratios, and logarithmically transformed bands of Landsat images has been tested. Scatter diagrams showed that several logarithmic and some linear models can describe the concentration of chlorophyll-a in Antikyra Bay. The 15 best linear models with the higher values of regression coefficient resulted from the satellite image of 5 September 2013 and were applied to images of 7 November 2013, 26 April 2014, 24 October 2014, 3 December 2014, 16 April 2015 and 6 October 2015 in order to determine which one is the most appropriate for assessing chlorophyll-a concentration in the bay.

3.2.1.) Correlations between spectral index and in situ concentration

Correlations between spectral index and in-situ chlorophyll-a concentration are summarized in the graph below. This diagram shows that OLI bands and spectral indices displayed differential sensitivity to chlorophyll-*a*.
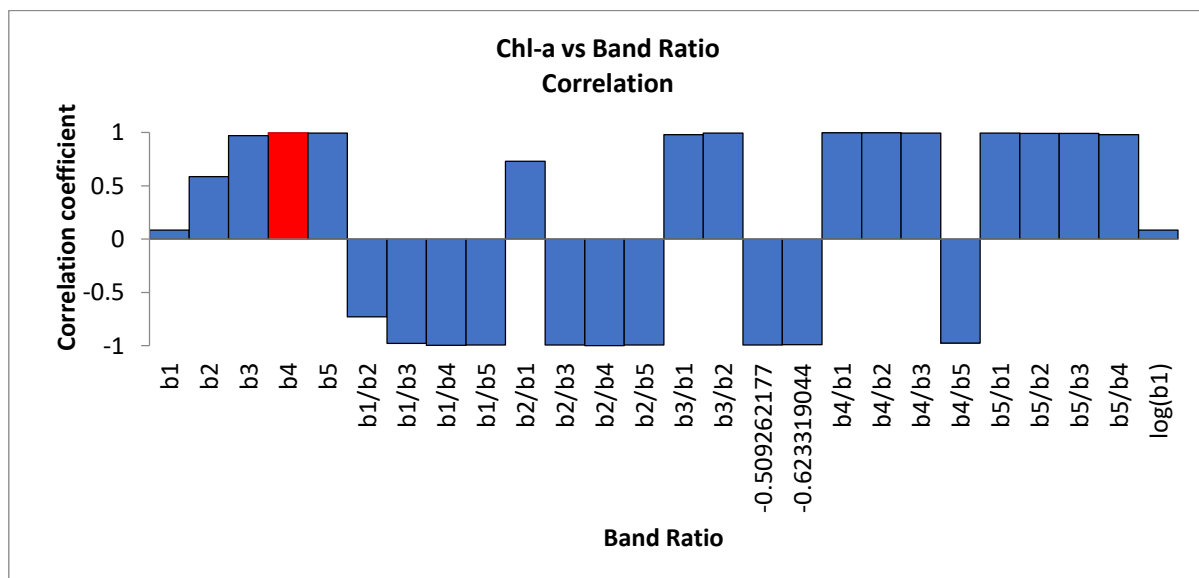

Fig.16.) Correlation coefficients between spectral index and chlorophyll-*a* concentration for 9 September 2013

In September 5th 2013, there was a significant correlation between reflectance value and in-situ chlorophyll-*a* concentration for all OLI bands from band 1 to 5. Band 3 (Green) and 4 (Red) were more sensitive than band 1 (Coastal aerosol), 2 (Blue) and 5 (Near Infrared).

There was a significant correlation between spectral indices including b3/b1, b3/b2, b4/b1, and b4/b2 and in-situ chlorophyll-a concentration; the spectral ratio index b4 (Red) /b1 (Coastal Blue) had the highest correlation with in-situ chlorophyll-a. The rest of the spectral indices did not show sensitivity to chlorophyll-a concentration.

Two scatter plot with high correlation (Fig.17.) and low correlation (Fig.18.) are shown below in order to emphasize the importance of the right band selection for the algorithm development.
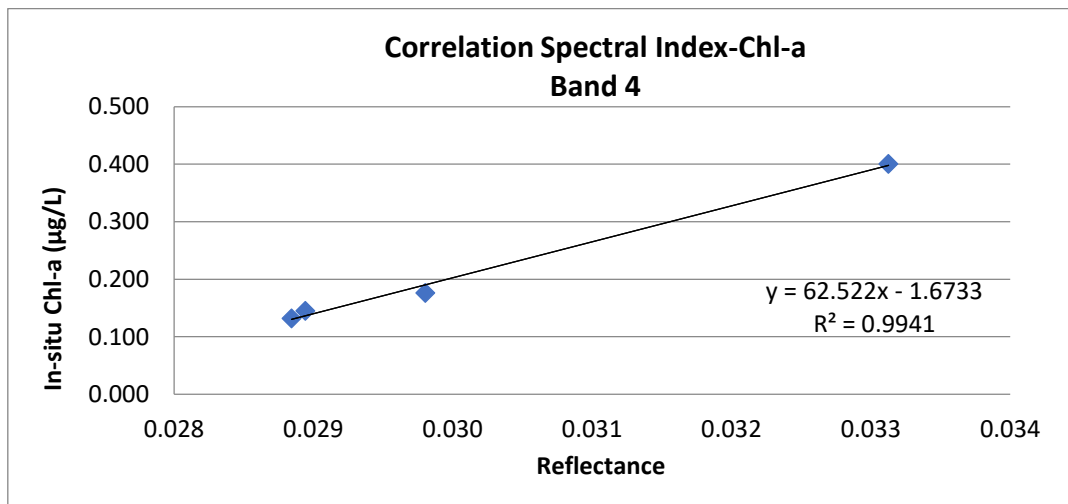

Fig.17.) Scatter plot for the spectral index of band 4 and the chlorophyll-*a* concentration indicating their correlation ad coefficient of determination
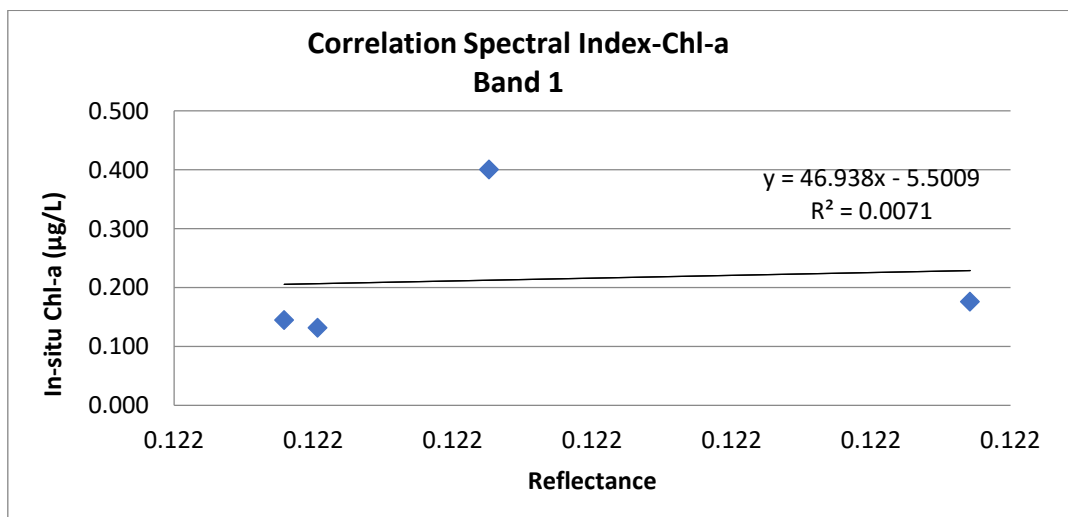
Fig.18.) Scatter plot for the spectral index of band 4 and the chlorophyll-*a* concentration indicating their correlation ad coefficient of determination

Watanabe et al. (2015) found that NIR-Red, NIR-Green and NIR-Blue ratios had an R^2 greater than 0.70 with in-situ chlorophyll-a concentration. This study results showed even higher coefficients of determination for the first 4 bands and their combinations. The high sensitivity in Red and Green may be due the fact there is negative reflectivity of chlorophyll-

a in the visible band, especially for red (Rundquist et al. 1996, Pepe et al. 2001). All tested band combinations with high determination coefficients are listed in the followed table:

Table 9.) Correlation between reflectance value and in-situ chlorophyll-a concentration for all OLI bands from band 1 to 5 and their combinations

Band Ratio	Correlation	Band Ratio	Correlation
b1	0.084400043924	log(b1)	0.084815994724
b2	0.587141107298	log(b2)	0.587286306878
b3	0.969111363148	log(b3)	0.967191235223
b4	0.997062594825	log(b4)	0.996110776669
b5	0.994746740706	log(b5)	0.994890154521
b1/b2	-0.728383949891	log(b1/b2)	-0.729081257744
b1/b3	-0.978014741257	log(b1/b3)	-0.979485502941
b1/b4	-0.997468885337	log(b1/b4)	-0.998160101376
b1/b5	-0.993591037476	log(b1/b5)	-0.993882858079
b2/b1	0.729820183143	log(b2/b1)	0.729123257179
b2/b3	-0.994667875825	log(b2/b3)	-0.995100459963
b2/b4	-0.998206844073	log(b2/b4)	-0.998493332941
b2/b5	-0.992619134684	log(b2/b5)	-0.992781312663
b3/b1	0.980889309620	log(b3/b1)	0.979484254823
b3/b2	0.995505822942	log(b3/b2)	0.995098514587
b3/b4	-0.992790944552	log(b3/b4)	-0.993236652633
b3/b5	-0.989878421945	log(b3/b5)	-0.990226455572
b4/b1	**0.998704431936**	log(b4/b1)	0.998160925593
b4/b2	0.998687169961	log(b4/b2)	0.998493062971
b4/b3	0.993626643456	log(b4/b3)	0.993235300287
b4/b5	-0.975828331574	log(b4/b5)	-0.978116191567
b5/b1	0.993823241212	log(b5/b1)	0.993883444286
b5/b2	0.992702037031	log(b5/b2)	0.992781039066
b5/b3	0.990413893126	log(b5/b3)	0.990227084150
b5/b4	0.980067837927	log(b5/b4)	0.978115436103

Table 10.) The 5 best band ratio correlations

Band Ratio	Correlation
b4/b1	0.998704432
b4/b2	0.998687170
log(b4/b2)	0.998493063
log(b4/b1)	0.998160926
b4	0.997062595

The 10 best linear and polynomial equations with the highest values of regression coefficient resulted from the satellite image of 5 September 2013 and were applied to images of 7 November 2013, 26 April 2014, 24 October 2014, 3 December 2014, 16 April 2015 and 6 October 2015 in order to determine which one is the most appropriate for assessing chlorophyll-a concentration in Antikyra Bay and the further area of Gulf of Corinth. The 5 most precise regression models and the algorithm which was used to convert reflectance values to Chl-a concentration (µg/L), are shown below:
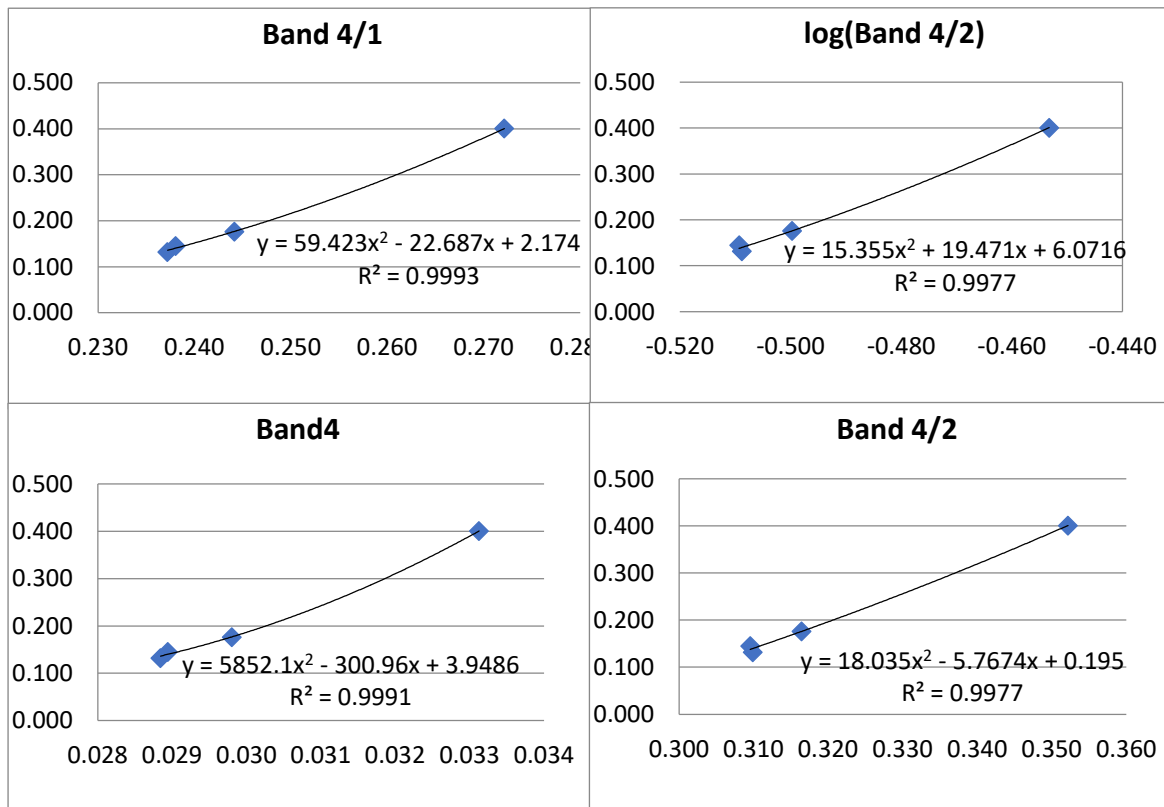

Fig.19.) Scatter plot for very precise regression models and their coefficient of determination
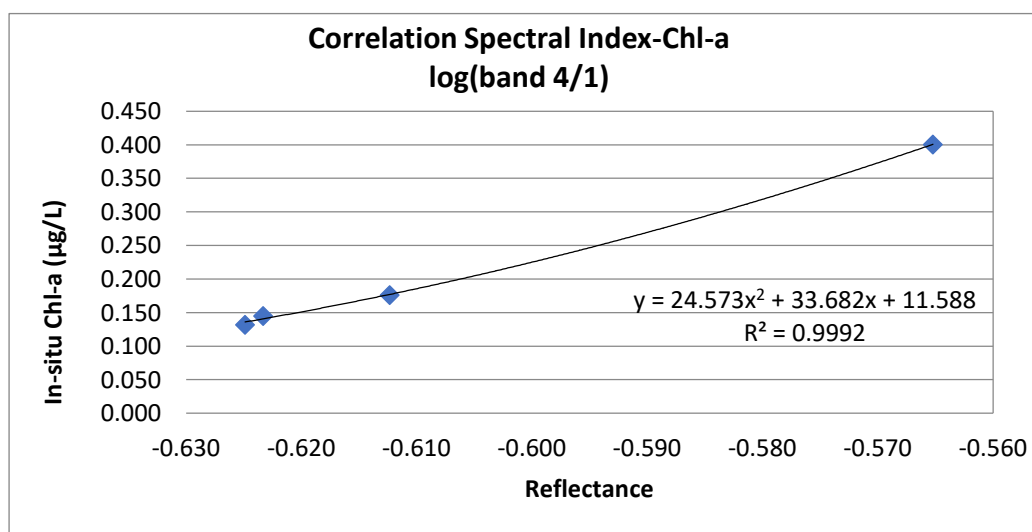

Fig.20.) Scatter plot for the most precise regression model

Based on the correlation coefficients above, the most sufficient local algorithm seems to be:

$$\text{chl-a } (\mu g/L) = 59.423x^2 - 22.687x + 2.174 \qquad (29)$$
$$x = Band(4/1)$$

Even though a limited number of sampling stations were available, equation (29) presented satisfying results for the modeled chlorophyll-a concentrations as shown below in the following tables:

Table 11.) In situ and the satellite-derived Chl-a measurements of each station for the first 3 dates

	05.09.2013	Landsat 8	08.11.2013	Landsat 8	26.04.2014	Landsat 8
Stations	Chl-a (µg/l)	Algorithm	Chla (µg/l)	Algorithm	Chla (µg/l)	Algorithm
A1	0.401	**0.400829**	0.162	**0.0864**	0.073	**0.0841**
A2	0.132	**0.136003**	0.134	**0.0701**	0.091	**0.0941**
A3	0.176	**0.177148**	0.179	**0.0796**	0.087	**0.0896**
A4	0.145	**0.140767**	0.178	**0.0875**	0.029	**0.0228**

Table 12.) In situ and the satellite-derived Chl-a measurements of each station for the next 4 dates

	24.10.2014	L 8	03.12.2014	L 8	16.4.2015	L 8	6.10.2015	L 8
Stations	Chla (µg/l)	Alg.	Chla (µg/l)	Alg.	Chla (µg/l)	Alg.	Chla (µg/l)	Alg.
A1	0.135	**0.1381**	0.257	**0.2993**	1.053	**0.5200**	0.395	**0.3579**
A2	0.098	**0.1035**	0.177	**0.1488**	0.479	**0.3966**	0.186	**0.2076**
A3	0.110	**0.0999**	0.168	**0.1522**	0.309	**0.2841**	0.176	**0.1723**
A4	0.147	**0.1987**	0.139	**0.1455**	0.234	**0.1681**	0.212	**0.2007**

The most stations presented values close to sampling ones. Hence, chlorophyll-a concentration maps were created according to equation (29) for each satellite image.
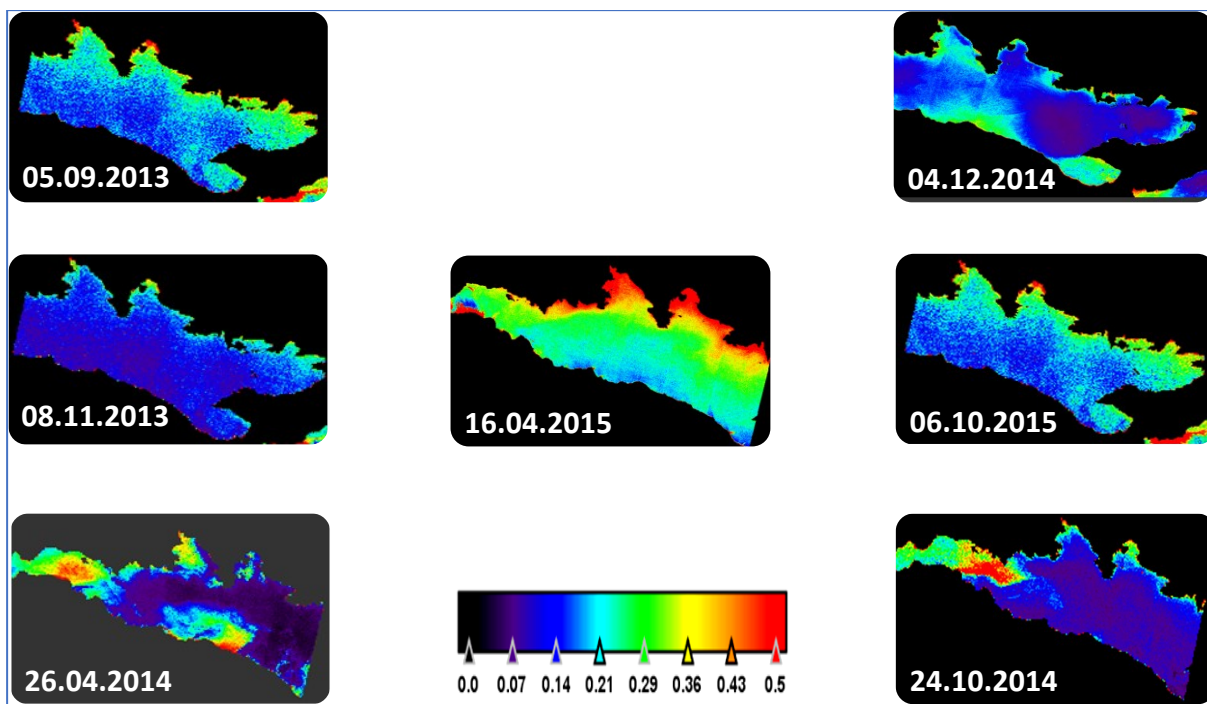
Fig.21.) Modeled chlorophyll-a concentrations based on the developed local algorithm for the available dates with in-situ measurements

The use of Landsat TM and ETM+ data for mapping Chl-a concentrations seems to be efficient with the application of an local algorithm. In order to examine the performance of the algorithm for operational monitoring, statistical comparison methods were used and are presented in (3.2.2.).

3.2.2.) Model Validation

A key criterion for selecting the best equation was originally the value of the coefficient of determination as resulted by the regression analysis between sampling values of chlorophyll-a concentration and the estimated digital numbers of the transformed satellite images at the available sampling stations. Furthermore, the algorithms performance was evaluated using the statistic metrics mentioned in (2.2.2.) based on the equations (20)-(24) and their normalized indexes: root mean squared error (RMSE), normalized root mean squared error (NRMSE), mean absolute percentage error (MAPE), PBIAS, NSE, mNSE, RSR correlation coefficient (Correl) and determination coefficient (R^2):

Table 13.) Statistic index values for the model simulation

Statistic index	Value	Goodness of fit	Statistic index	Value	Goodness of fit
RMSE	0.11	Perfect=0	PBIAS	16.49	<25%
NRMSE	0.10	Perfect=0	NSE	0.67	>0.5
MAPE	0.17	Perfect=0	mNSE	0.60	>0.5
Correl	0.88	Exact=1	RSR	0.57	<0.70

In general, model simulation can be judged as satisfactory if NSE > 0.50 and RSR < 0.70, and if PBIAS <25% based on Moriasi et al. (2007). In addition a Taylor diagram has been used in order to summarize the relative skill with which the model simulates the pattern of the chlorophyll-a concentration.
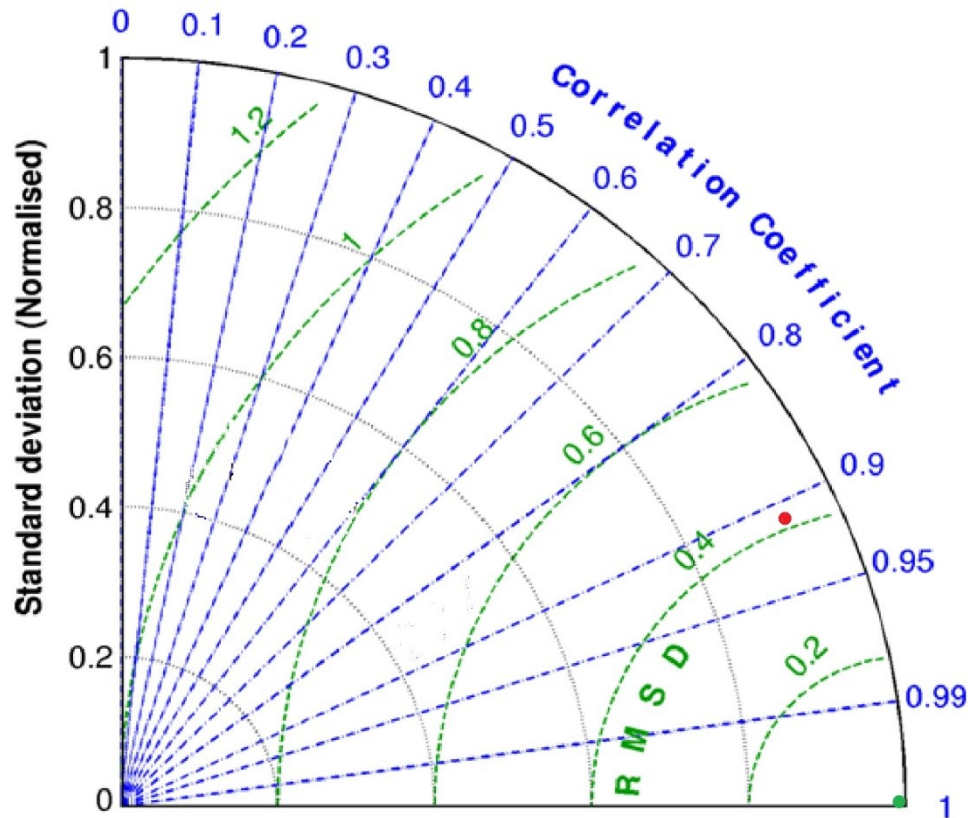

Fig.22.) Taylor diagram displaying the statistical comparison with observations of in-situ chlorophyll-a concentrations in Antikyra Bay

The position of the red dot on the plot quantifies how closely the model's simulated concentration pattern matches the observations. Its pattern correlation with observations is about 0.91. The centered root-mean-square (RMS) difference between the simulated and observed patterns is proportional to the distance to the point on the x-axis identified as "observed." The green contours indicate the RMS values and it can be seen that in the case of the used algorithm the centered RMS error is about 0.32 μg/L. The standard deviation of the simulated pattern is proportional to the radial distance from the origin.

In general, it seems that all used statistic indexes indicate a successful simulation. In addition, as it can be seen in the graph below, it seems that one in-situ concentration is much higher than the majority of the samplings. This high concentration doesn't exist in the simulated dataset. This fact may indicate some unusual event like e.q., some phytoplankton plume on the specific date (16.04.2014) and time, since the satellite data was received at a different time (09:10 am) on which the concentration may have not yet increased this much.
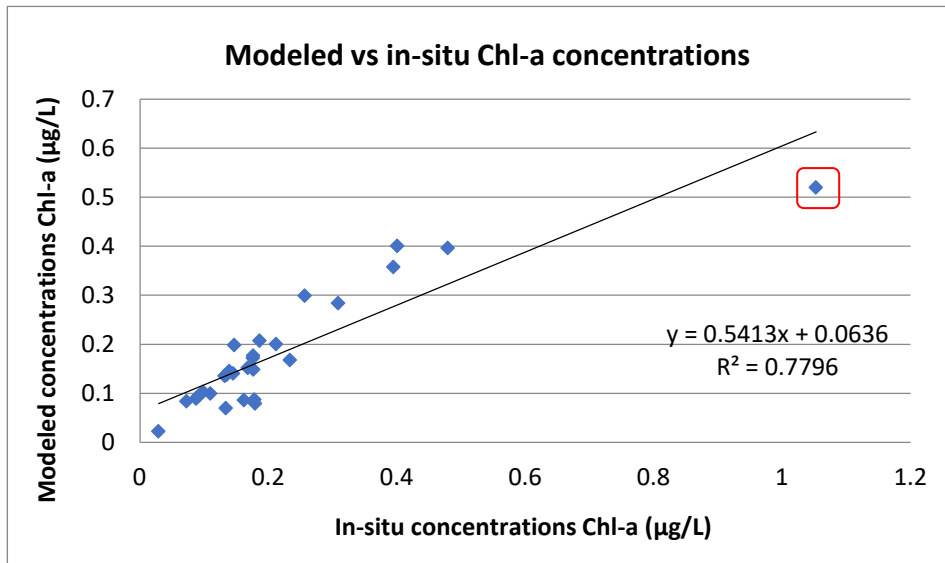
Fig.22.) Scatter plot of the modeled and in-situ chlorophyll-a concentrations indicating the unusual high in-situ concentration

3.3.) Heat Flux

In the graph below (Fig.23.) air-sea flux data from the National Centers for Atmospheric Prediction (NCEP) and the National Center for Atmospheric Research (NCAR) are represented. These time series were used to estimate the net air to sea heat flux in the region of Antikyra bay during the years 1960 (when the aluminum plant was established) and 2017.
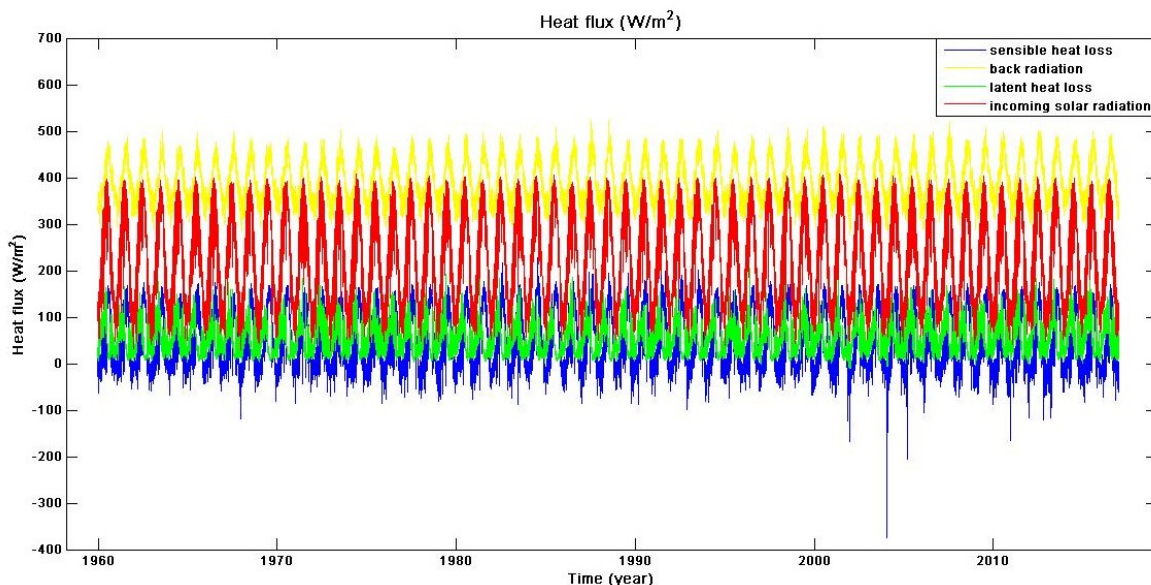

Fig. 23.) Seasonal evolution of air-sea flux data from the National Centers for Atmospheric Prediction (NCEP) and the National Center for Atmospheric Research (NCAR). Positive values represent upward heat flux (heat loss by the sea), except in the case of solar radiation.

The flux data represents the net of the incoming solar radiation, back radiation, latent and sensible heat loss:

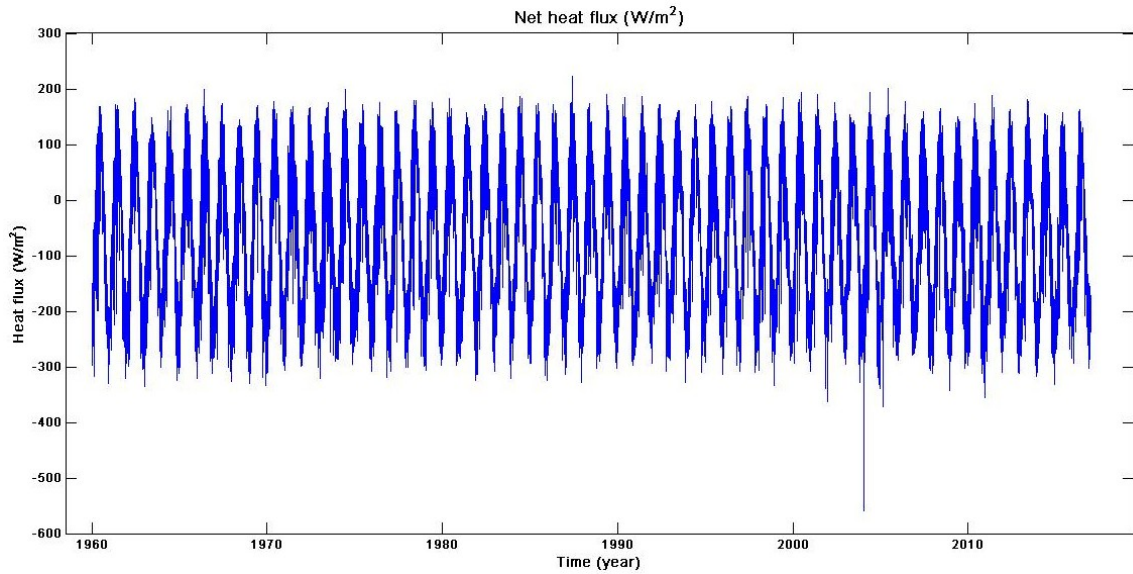Figure 24.) Temporal evolution of net heat flux from the sea surface in the atmosphere.
Here, positive values indicate heat gain by the sea.

Furthermore, in order to compare the single heat fluxes with the estimated results of the sea surface temperature and chlorophyll-a concentration, the fluxes were estimated again for the last 20 years.
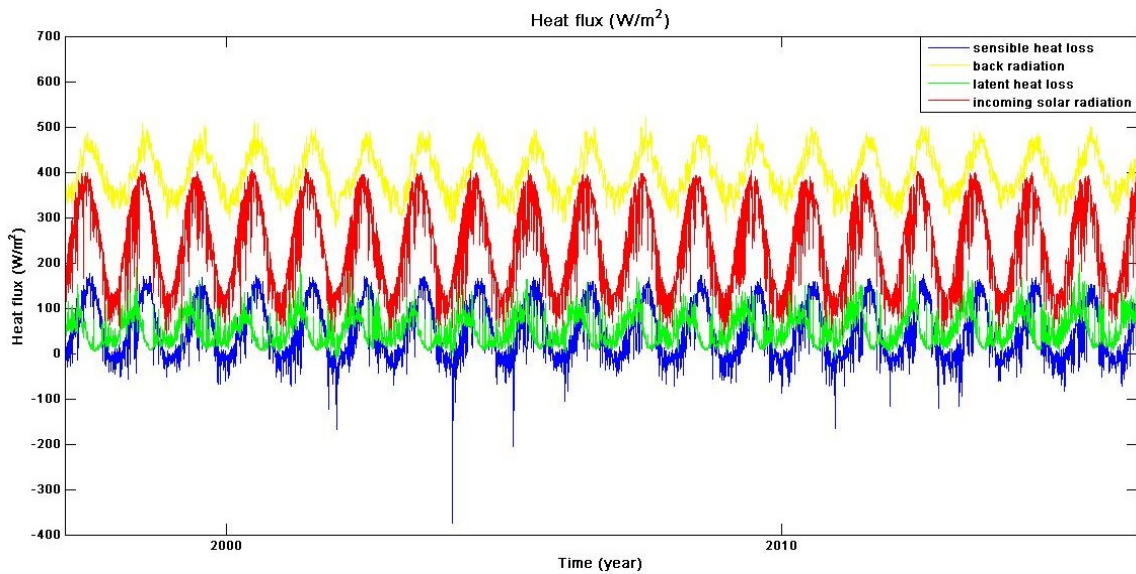
Fig. 25.) Temporal evolution of all heat flux data for the last twenty years
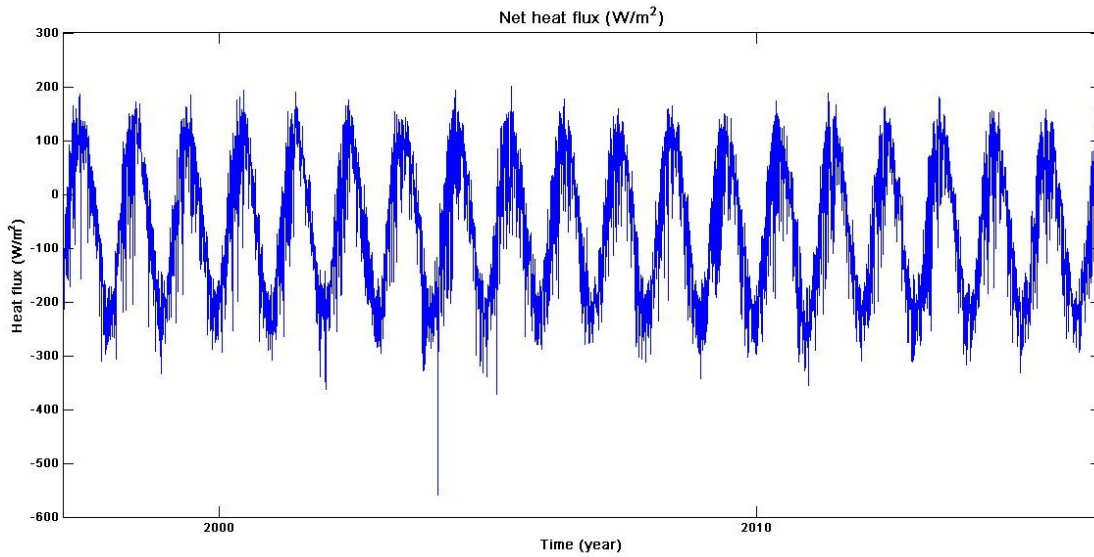
Fig. 26.) Temporal evolution of net heat flux from the sea surface for the last twenty years

3.4.1.) Heat flux influences on sea surface temperature

In order to analyze how the atmosphere influences the SST variation, the comparison of the net air-sea heat flux and the different radiations and heat losses with sea surface temperature are presented in the graphs below.

Fig. 27.) Comparison graph of net heat flux and sea surface temperature

Also, the comparison of the components of heating due to short-wave radiation, outgoing long-wave radiation, sensible heat flux, and latent heat flux and the sea surface temperature are shown below:

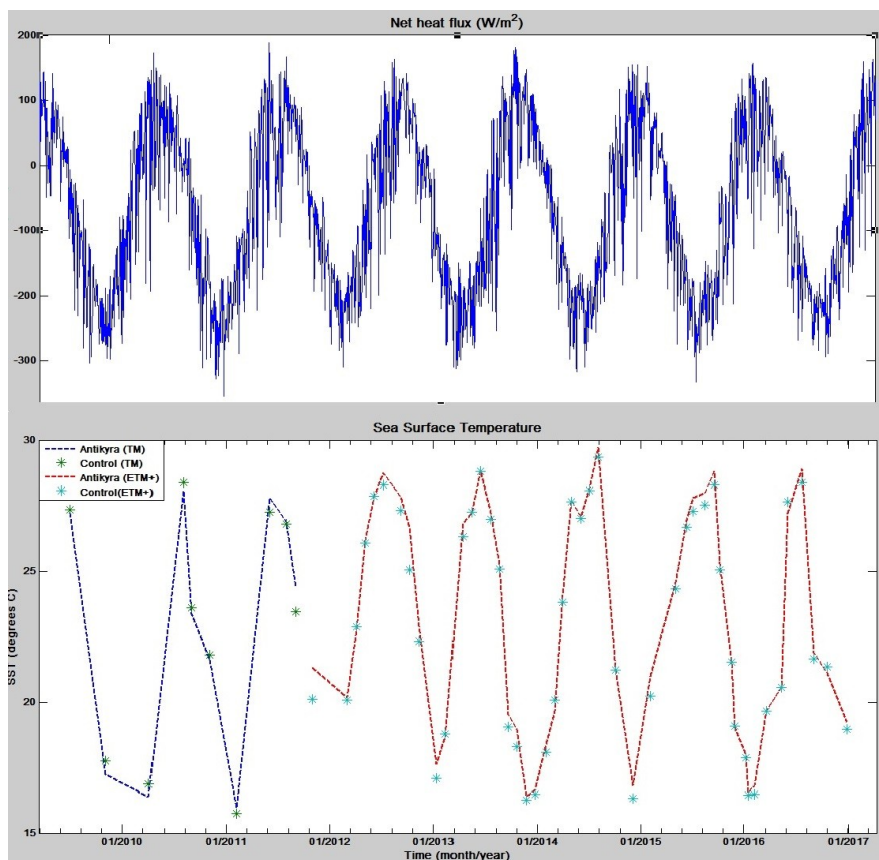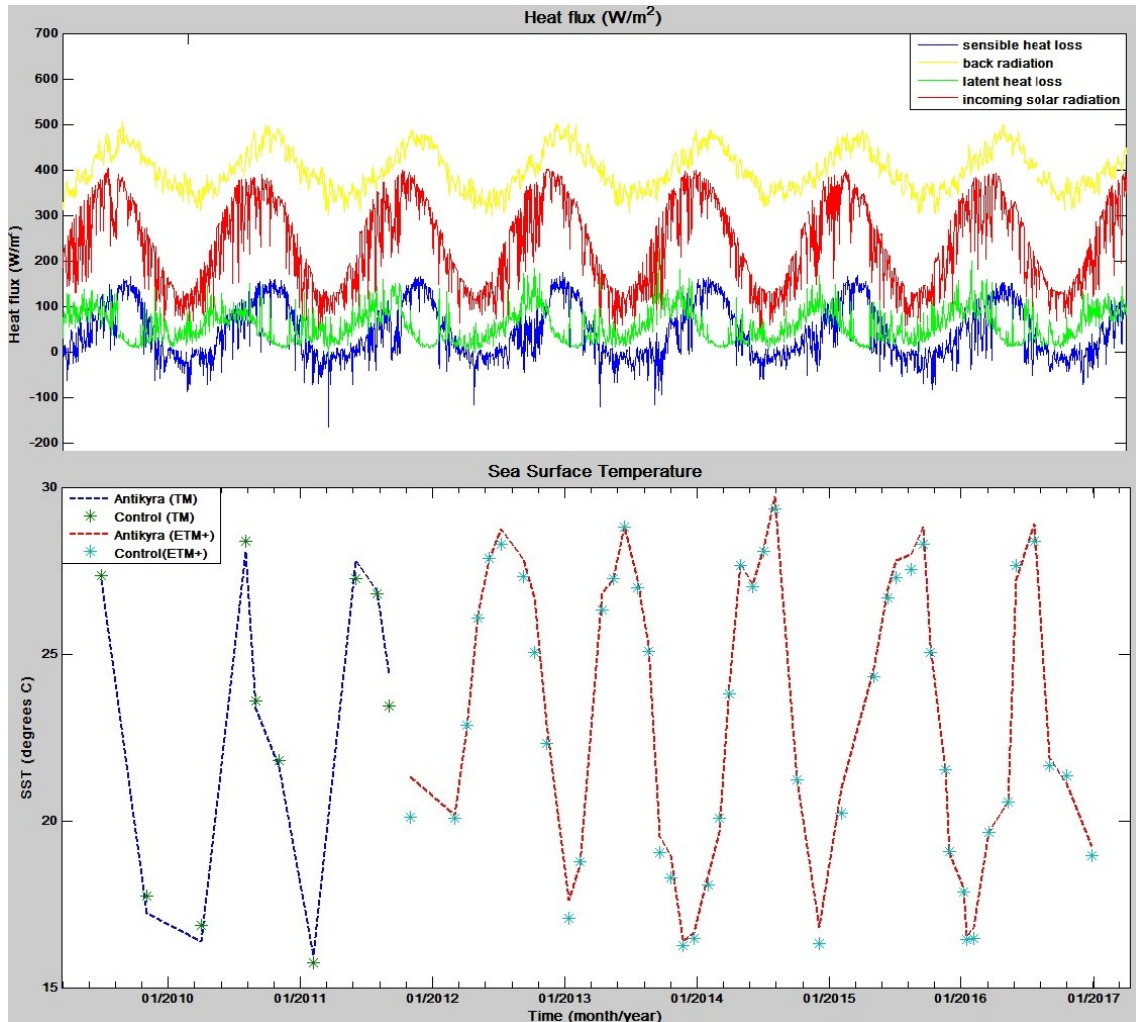Fig. 28.) Comparison graph of all heat flux components and sea surface temperature

Figure 27 indicated that the sea surface temperature and the net heat flux vary similarly. For better investigation of the atmospheric influences on the SST variation the results of the application of Frankignouls' method based on the equations (26)-(28) are shown below.

The feedback of the surface heat flux (α) is estimated for each three consecutive monthly periods. For each season the factor α (W/m^2/°C) is estimated using consecutive three months of daily data of the net heat flux (Q_{surf}) and the sea surface temperature (SST) time series.

Table 14.) Estimated heat flux feedback over the gulf of Corinth

Feedback factor	Winter (JFM)	Spring (AMJ)	Summer (JAS)	Autumn (OND)
α	-2.2	4.3	1.7	-2.4

The negative factor α for the winter season indicates a positive surface heat flux feedback (equation 26). During this period, the ocean responses to the cooling by releasing heat to the atmosphere. In spring, from April to June, the factor α remains high and positive and the feedback is negative which indicates that the ocean probably storages energy. During summer factor α is low, the atmosphere has less influence on the SST anomalies.

4.) Conclusion and Discussion

In this study the sea surface temperature estimation, based on thermal infrared (TIR) remote sensing from satellite images of Landsat Thematic Mapper (TM) and Landsat Enhanced Thematic Mapper (ETM+) revealed satisfying results. This fact enabled the investigation of a potential thermal pollution due to an aluminum plant in Antikyra Bay in the Gulf of Corinth. The results indicated with statistical significance that no thermal effluent of the cool hot cooling water from the aluminum plant were detectable. This could be explained by the presence of a wastewater treatment system in the area of Agios Nikolaos. The processed cold freshwater from the treatment system and the warm cooling water from the aluminum plant reduce the impact of each other in the area of Antikyra Bay based on the results of the National Monitoring Project of Greece from the Hellenic Centre for Marine Research. Furthermore, the sea surface temperature estimation enabled the seasonal surface temperature variation mapping which revealed a strong seasonal signal.

In addition, a local algorithm for estimating Chlorophyll-a concentration based on high analysis Landsat 8 data was developed for the area of the Gulf of Corinth. This method was based on band rationing and regression modeling, established from in-situ measurements and satellite images. Chlorophyll-*a* samples which have been collected by the Hellenic Centre for Marine Research at 4 different stations, in Antikyra Bay from April 2014 until October 2015 and satellite images of Landsat 8 of the same area were used in order to statistically correlate the in-situ measurements with various combinations of Landsat bands in order to quantify algorithms that best describe this relationship and calculate accurately the concentration of chlorophyll-a. Several models were used to examine these relationships which included linear, exponential and log transformations. The combination of band 4 and band 1 showed the most significant ratio in estimating chlorophyll-a with a maximum correlation coefficient of $R^2 = 0.99$. Based on the correlation coefficients, the most sufficient local algorithm was found to be chl-a= $59.423(band4/1)^2$-22.687(band4/1)+2.174. Even though a limited number of sampling stations were available, the selected equation presented strongly satisfying results. The algorithm was applied to other satellite images of different dates but with available in-situ chl-*a* data, in order to validate the results. Satellite derived chlorophyll-*a* values were compared to *in-situ* chlorophyll-*a* values originated from other past scientific studies. The initial results confirmed the suitability of the method for assessing the concentration of chlorophyll-*a* in the Gulf of Corinth with relative accuracy when no field data are available.

The last section indicates the atmosphere influences on the sea surface temperature variation based on the analyzed heat fluxes. It is known that the warming of water is induced by solar heating. The fact that the shortwave radiation flux (SH) increases from March to May and achieves its maximum in May-June indicates that the increase of the sea surface temperature during the same period is strongly related. However, wind speed decreases and shows a minimum in May based on the local meteorological data (WMO). This indicates that during a low wind period, solar heating probably induces a rise in air and sea surface

temperature and the thermal system can't be described so easily. Furthermore, these results are based on satellite data of the surface water, and in-situ measurements in the water column waters are required for a better understanding of the mechanisms that govern the thermal structures in this area.

5.) Data Resources

Bathymetry data

The bathymetry data have been derived from the European Marine Observation and Data Network (EMODnet) Bathymetry portal (http://www.emodnet-bathymetry.eu.) and it have been analyzed and presented with the GeoMapApp which is available in the through the visualization software suite from the Marine Geoscience Data System (www.geomapapp.org/html/help/exportSD.html).

Air-sea flux data

Air-sea flux data have been derived from the National Center for Atmospheric Prediction (NCEP) and the National Center for Atmospheric Research (NCAR) daily reanalysis (*http://www.esrl.noaa.gov/psd/*) and were used to examine time-series of air-sea fluxes and heat loss using Matlab R2013a. The data assimilation system uses a 3D-variational analysis scheme, with 28 sigma levels in the vertical and a triangular truncation of 62 waves which corresponds to a horizontal resolution of approximately 200 km Kalnay et. al, 1996). A forecast from the NCEP global spectral model was used as the first-guess fields for this reanalysis.

Satellite data

In this study satellite images of Landsat Thematic Mapper (TM) from Landsat 5, Landsat Enhanced Thematic Mapper (ETM+) from Landsat 7, and Landsat Operational Land Imager (OLI) and Thermal Infrared Sensor (TIRS) of Landsat 8 were used. The data were acquired for all available images with less than 20% cloud cover from 10.2009 until 12.2016 from the United States Geological Survey (USGS) (https://earthexplorer.usgs.gov/).

Chlorophyll-a field data

The chlorophyll-a concentrations for 4 different stations and for 6 different dates (from April 2014 to October 2015) in the area of Antikyra Bay were provided by Prof. Asimakopoulou from the Hellenic Center for Marine Research (H.C.M.R) (http://www.hcmr.gr/en/).

6.) References

Allan J and Castillo M, 2007. Stream Ecology: Structure and Function of Running Waters. Dordrecht, Springer.

Anderson J and Carmack C, 1973. Some physical and chemical properties of the Gulf of Corinth. *Estuar. coast. mar. Sei.* 1: 195-202.

Andreadis T, Avgoustoglou E, Galanis G, Fragouli V, 2001. Use and Verification of ECMWF products in Greece. *Verification of ECMWF products in Member States and Co-operating States, Report 200, European Center for Medium-Range Weather Forecasts*: 50.

Barsi J, Lee K, Kvaran G, Markham B, Pedelty J, 2014. The Spectral Response of the Landsat-8 Operational Land Imager. *Remote Sens. 6*: 10232-10251.

Bilge F, Yazici B, Dogeroglu T, Ayday C, 2003. Statistical evaluation of remotely sensed data for water quality monitoring. International Journal of Remote Sensing, 24: 5317-5326.

Boyer J, Kelble C, Ortner P, Rudnick D, 2009. Phytoplankton bloom status: Chlorophyll a biomass as an indicator of water quality condition in the southern estuaries of Florida, USA. *Ecol. Indic*. 9: S56–S67.

Cardoso-Mohedano J, Bernardello R, Sanchez-Cabeza J, Molino M, Ruiz-Fernández A, Cruzado A, 2015. Accumulation of conservative substances in a sub-tropical coastal lagoon. *Estuarine Coastal and Shelf Science:* 164.

Cairns J, 1971. Thermal pollution a cause for concern, *Water Pollut. Control Fed.* 1: 55-66.
Cheng A, Wei Y, Lv G, Yuan Z, 2013. Remote estimation of chlorophyll-a concentration in turbid water using a spectral index: A case study in Taihu Lake, China. *J. Appl. Remote Sens.*

Coll C, Galve J, Sánchez J, Caselles V, 2010. Validation of Landsat-7/ETM+ Thermal-Band Calibration and Atmospheric Correction with Ground-Based Measurements. *IEEE Trans. Geosci. Remote Sens.* 48 (1): 547–555.

Choi B and Wilkin J, 2007. The effect of wind on the dispersal of the Hudson River plume. *J. Phys. Oceanogr*.37: 1878–1897.

Davis J, 2006. Advances in hydropower technology can protect the environment, alternative energy sources: 82–87. Detroit: Greenhaven.

Eva H and Lambin E, 1998. Burnt area mapping in Central Africa using ATSR data, *International Journal of Remote Sensing* 19: 3473-3497.

Erkkilä A, and Kalliola R, 2004. Patterns and dynamics of coastal waters in multi-temporal satellite images: support to water quality monitoring in the Archipelago Sea, Finland. *Estuarine, Coastal and Shelf Science,* 60(2): 165-177.

Ferentinos G, Papatheodorou G, Geraga M, Christodoulou D, Fakiris E, Iatrou M, 2015: The Disappearance of Helike-Classical Greece- New Remote Sensing and Geological Evidence, *Remote Sensing* 7: 1263-1278.

Friligos N, Theocharis A, Georgopoulos D, 1985. Preliminary chemical and physical observations during sommer 1980 on a silled embayment in the Ionian sea. Vie Milieu 35 (2): 115-125.

Fourniotis N, Horsc M, 2012. Early summer circulation in the Gulf of Patras (Greece). *Isope* 4:740-745.

Frankignoul C, Czaja A, L Heveder B, 1998. Air-sea feedback in the North Atlantic and surface boundary conditions for ocean models. *J Clim* 11: 2310-2324.
Giardino, C., Pepe, M., Brivio, P.A., Ghezzi, P. and Zilioli. E., 2001. Detecting chlorophyll, Secchi disk depth and surface temperature in a sub-alpine lake using Landsat imagery. *The Science of The Total Environment,* 268(1-3): 19-29

Han L and Jordon K, 2005. Estimating and mapping chlorophyll-a concentration in Pensacola Bay, Florida using Landsat ETM+ data. *Intl. J. Remote Sensing* 26(23): 5242-5254.

Handcock R, Torgersen C, Cherkauer K, Gillespiel A, Tockner K, Faux R , Tan J, 2012.Thermal infrared remote sensing of water temperature in riverine landscapes. *Fluvial Remote Sensing for Science and Management:* 85-112.

He R, Chen K, Moore T, Li M, 2006. Mesoscale variations of sea surface temperature and ocean color patterns at the Mid-Atlantic Bight shelfbreak. *Geophys. Res. Lett.* 37 (9).

Hellweger, Schlosser, Lall U, Weissel J, 2004. Use of satellite imagery for water quality studies in New York Harbor. *Estuarine, Coastal and Shelf Science* 61(3): 437-448.

Heezen B, Glass B, Menard H, 1966. Annotated record of the detailed examination of Mn deposits from R/V Vema Cruise 18 in the Manihiki Plaeau area, Pacific Ocean. *Deep Sea Research and Oceanographic Abstracts* 13 (3): 445-458.

Kabbara N, Benkheil J, Awad M, Barale V, 2008. Monitoring water quality in the coastal area of Tripoli (Lebanon) using high-resolution satellite data. *ISPRS Journal of Photogrammetry & Remote Sensing*, 63: 488–495.

Kalnay E, Kanamitsu M, Kistler R, Collins W, Deaven D, Gandin L, Iredell M, Saha S, White G, Woollen J, Zhu Y, Leetmaa A, Reynolds R, Chelliah M, Ebisuzaki W, Higgins W, Janowiak J, Mo K, Ropelewski C, Wang J, Jenne R, Joseph D, 1996. The NCEP/NCAR 40-Year Reanalysis Project, *Bull. Amer. Meteorol. Soc,* 77 (3): 437–471.

Keiner L and Yan X, 1998. A Neural network model for estimating sea surface chlorophyll and sediments from Thematic Mapper imagery. *Remote Sens. Environ.* 66: 153-165.

Kulkarni A, 2011. Water Quality Retrieval from Landsat TM Imagery. *Procedia Computer Science* 6: 475-480.

Langfort T, 1990. Ecological Effects of Thermal Discharges, *Elsevier Applied Science* :1-6.

Lascaratos A, Salusti E, Papageorgaki G, 1989. Wind induced upwellings and currents in the Gulfs of Patras, Nafpaktos and Korinthos, Western Greece. *Oceanologica Acta,* 12(3): 159-164.

Le C, Hu C, Jennifer C, David E, Frank M, Lee Z, 2013. Evaluation of chlorophyll-a remote sensing algorithms for an optically complex estuary. *Remote Sens. Environ*. 129: 75–89.

Loveland T and Dwyer J, 2012. Landsat: building a strong future. Remote *Sens. Environ.* 122: 22–29.

Markham B and Helder D, 2012. Forty-year calibrated record of earth-reflected radiance from Landsat: a review. *Remote Sens. Environ.* 122: 30–40.

Morgan I and Carpenter R, 1978. Biocides. Power Plant Entrainment—A Biological Assessment. Academic Press, Inc., New York: 96–113

Moretti I, Lykousis V, Sakellariou D, Reynaud J, Benziane B, Prinzhoffer A, 2004. Sedimentation and subsidence rate in the Gulf of Corinth: what we learn from the Marion Dufresne's long piston coring. C.R. *Geoscience* 336: 291-299.

Moriasi D, Arnold J, VanLiew M, Bingner R, Harmel R, Veith T, 2007. Model Evaluation Guidelines for Systematic Quantification of Accuracy in Watershed Simulations. *Transactions of the ASABE*, 50: 885-900.

National Land Archive Production System (NLAPS) Systematic Format Description Document – U.S. Geological Survey Format Specifications for Geometrically Corrected Landsat L1 Digital Data Products, July 2000.

Nazeer M and Nichol J, 2016. Development and application of a remote sensing-based chlorophyll-a concentration prediction model for complex coastal waters of Hong Kong. Journal of Hydrology 532:80-89

Nielsen J, 1912. Hydrography of the Mediterranean and adjacent waters. *Rep. Dan. Oceanogr. Exp. Medit*. 1: 77–192.

Pan G, Tang D, Zhang Y, 2012. Satellite monitoring of phytoplankton in the East Mediterranean Sea after the 2006 Lebanon oil spill. *Int. J. Remote Sens.* 33: 7482–7490.

Papageorgiou M, 2016. Coastal and marine tourism: a challenging factor in Marine Spatial Planning, *Ocean and Coastal Management* 129: 44-49.

Paul M and Meyer J, 2001. Streams in the urban landscape. *Annu. Rev. Ecol. Syst.* 32: 333-65.

Poff N, Allan J, Bain M, Karr J, Prestegaard K, Richter B, Sparks R, Stromberg J, 1997. The natural flow regime: a paradigm for river conservation and restoration. *BioScience,* 47: 769-784.

Pepe M, Giardino C, Borsani G, Cardoso A, Chiaudani G, Premazzi G, Rodari E, Zilioli E, 2001. Relationship between apparent optical properties and photosynthetic pigments in the subalpine Lake Iseo. *The Science of The Total Environment* 268 (1): 31-45.

Piper D, Kontopoulos N, Anagnostou C, Chronis G, Panagos A, 1999. Modern fan deltas in the western Gulf of Corinth, Greece. *Geo-Marine Letters* 10: 5-12.

Poole G and Berman C, 2001. Ecological Perspective on In-Stream Temperature: Natural Heat Dynamics and Mechanisms of Human-Caused Thermal Degradation. *Environmental Management 27* (6):787-802.

Poulos S, Collins M, Pattiaratchi C, Cramp A, Gull W, Tsimplis M, Papatheodorou G, 1996. Oceanography and sedimentation in the semi-enclosed, deep-water Gulf of Corinth (Greece),*Marine Geology* 134: 213-235.

Pluhowski E, 1970. Urbanization and its effect on the temperature of the streams in Long Island, New York. U.S. Geological Survey, *Professional Paper 627-D. U.S. Geological Survey.*

Rahul S and Gnanaseelan C, 2013. Net Heat Flux Over the Indian Ocean: Trends, Driving Mechanisms, and Uncertainties. *Iee Geoscience and Remote Sensing Letters*, 10 (4): 776-780.

Raithby G, Stubley D, Taylor P, 1988. The Askervein Hill project: a finite control volume prediction of three-dimensional flows over the hill*. Boundary-Layer Meteorology* 39: 247–267.

Ryan W, Carbotte J, Coplan S, O'Hara A, Melkonian R, Arko R, Weissel V, Ferrini A, Goodwillie F, Nitsche F, Bonczkowski J and R. Zemsky R, 2009. Global Multi-Resolution Topography (GMRT) synthesis data set, *Geochem. Geophys. Geosyst.*, 10: Q03014.

Rundquist D, Han L, Schalles J, Peake J, 1996. Remote measurement of algal chlorophyll in surface waters: the case for the first derivative of reflectance near 690 nm. *Photogrammetric Engineering & Remote Sensing,* 62 (2): 195-200.

Salgueiro V, Costa M, Silva A, Bortoli D, 2015. Effects of clouds on the surface shortwave radiation at a rural inland mid-latitude site. *Atmos. Res. 178-179*: 95-101.

Stathopoulou M, and Cartalis C, 2007. Daytime urban heat islands from Landsat ETM+ and Corine land cover data: an application to major cities in Greece. *Solar Energy* 81, (3):358–368.

Sun D, Hu C, Qiu Z, Cannizzaro J, Barnes B, 2014. Influence of a red band-based water classification approach on chlorophyll algorithms for optically complex estuaries. *Remote Sens. Environ.* 155: 289–302.

Sudheer K, Chaubey I, Garg V, 2006. Lake water quality assessment from Landsat thematic Mapper data using neural network: an approach to optimal band combination selection. *Journal of the American Water Resources Association*: 1683-1695.

Taylor K, 2001. Summarizing multiple aspects of model performance in a single diagram. Journal of Geophysical Research-Atmospheres, V106, D7.

Topouzelis K, Varnava S, Georgiou A, 2012. Spatial and temporal mapping of SST in east mediterranean (Aegean Sea) during 2005–2008. *Geoscience and Remote Sensing Symposium (IGARSS), 2012 IEEE International:* 2617-2620.

Torbick N, Hessionb S, Hagena S, Wiangwang N, Beckerc B, Qi J, 2013. Mapping inland lake water quality across the Lower Peninsula of Michigan using Landsat TM imagery. *International Journal of Remote Sensing* 34(21): 7607-7624.

Wang Y, Jiang H, Jin J, Zhang X, Lu X, Wang Y, 2015. Spatial-temporal variations of Chlorophyll-a in the adjacent sea area of the Yangtze River estuary influenced by Yangtze River discharge. *Int. J. Environ. Res. Public Health* 12: 5420–5438.

Watanabe F, Alcântara E, Rodrigues T, Imai N, Barbosa C, Rotta L, 2015. Estimation of Chlorophyll-a Concentration and the Trophic State of the Barra Bonita Hydroelectric Reservoir Using OLI/Landsat-8 Images. *Int J Environ Res Public Health*, 12(9): 10391-417.

Xing Q and Chen C, 2006. Method of integrating Landsat-5 and Landsat-7 data to retrieve sea surface temperature in coastal waters on the basis of local empirical algorithm. *Ocean Science Journal* 41: 97-104.

Xu H, Chen B, 2004. Remote sensing of the urban heat island and its changes in Xiamen City of SE China. *Journal of Environmental Sciences* 16 (2): 276–281.

Zhang Y, Koponen R, Pulliainen J, Hallikainen M, 2003. Application of empirical neural networks to chlorophyll a estimation in coastal waters using remote optosensors. IEEE *Sensors J.,* 3: 376-382.

Reports

NCEP/NCAR 40-Year Reanalysis Project: March, 1996 BAMS

EMODnet Bathymetry Consortium (2016): EMODnet Digital Bathymetry (DTM).

The 9th Sustainability Report 2016 of MYTILINEOS Group, available at http://www.mytilineos.gr/Uploads/ETHSIA_DELTIA/csr_reports/Sustainability_Report_2016_EN.pdf

Archipelagos N.G.O, Introduction to the marine fauna and flora of the Corinthian Gulf. (In Greek). Available at: http://korinthiakos.info/content